



HAL
open science

A patchy CO₂ exosphere on Ganymede revealed by the James Webb Space Telescope

Dominique Bockelee-Morvan, Olivier Poch, François Leblanc, Vladimir Zakharov, Emmanuel Lellouch, Eric Quirico, Imke de Pater, Thierry Fouchet, Pablo Rodriguez-Ovalle, Lorenz Roth, et al.

► **To cite this version:**

Dominique Bockelee-Morvan, Olivier Poch, François Leblanc, Vladimir Zakharov, Emmanuel Lellouch, et al.. A patchy CO₂ exosphere on Ganymede revealed by the James Webb Space Telescope. Astronomy and Astrophysics - A&A, In press, 10.1051/0004-6361/202451599 . insu-04733988v1

HAL Id: insu-04733988

<https://insu.hal.science/insu-04733988v1>

Submitted on 13 Oct 2024 (v1), last revised 27 Oct 2024 (v2)

HAL is a multi-disciplinary open access archive for the deposit and dissemination of scientific research documents, whether they are published or not. The documents may come from teaching and research institutions in France or abroad, or from public or private research centers.

L'archive ouverte pluridisciplinaire **HAL**, est destinée au dépôt et à la diffusion de documents scientifiques de niveau recherche, publiés ou non, émanant des établissements d'enseignement et de recherche français ou étrangers, des laboratoires publics ou privés.



Distributed under a Creative Commons Attribution 4.0 International License

LETTER TO THE EDITOR

A patchy CO₂ exosphere on Ganymede revealed by the James Webb Space Telescope

Dominique Bockelée-Morvan¹, Olivier Poch², François Leblanc³, Vladimir Zakharov¹, Emmanuel Lellouch¹, Eric Quirico², Imke de Pater^{4,5}, Thierry Fouchet¹, Pablo Rodriguez-Ovalle¹, Lorenz Roth⁶, Frédéric Merlin¹, Stefan Duling⁷, Joachim Saur⁷, Adrien Masson¹, Patrick Fry⁸, Samantha Trumbo⁹, Michael Brown¹⁰, Richard Cartwright¹¹, Stéphanie Cazaux¹², Katherine de Kleer¹⁰, Leigh N. Fletcher¹³, Zachariah Milby¹⁰, Audrey Moingeon², Alessandro Mura¹⁴, Glenn S. Orton¹⁵, Bernard Schmitt², Federico Tosi¹⁴, and Michael H. Wong⁴

¹ LESIA, Observatoire de Paris, Université PSL, Sorbonne Université, Université Paris Cité, CNRS, 92195, Meudon, France, e-mail: Dominique.Bockelee@obspm.fr

² Univ. Grenoble Alpes, CNRS, IPAG, 38000 Grenoble, France

³ LATMOS/CNRS, Sorbonne Université, UVSQ, Paris, France

⁴ Department of Astronomy, University of California, 22 Berkeley, CA 94720, USA

⁵ Department of Earth and Planetary Science, University of California, 22 Berkeley, CA 94720, USA

⁶ Space and Plasma Physics, KTH Royal Institute of Technology, Stockholm, Sweden

⁷ Institute of Geophysics and Meteorology, University of Cologne, Albertus Magnus Platz, 50923 Cologne, Germany

⁸ University of Wisconsin, Madison, WI, 53706, USA

⁹ Department of Astronomy & Astrophysics, University of California, San Diego, La Jolla, CA 92093, USA

¹⁰ Division of Geological and Planetary Sciences, Caltech, Pasadena, CA 91125, USA

¹¹ Johns Hopkins University Applied Physics Laboratory, 11001 Johns Hopkins Rd. Laurel, MD 20723, USA

¹² Faculty of Aerospace Engineering, Delft University of Technology, Delft, The Netherlands

¹³ School of Physics and Astronomy, University of Leicester, University Road, Leicester, LE1 7RH, UK

¹⁴ Istituto Nazionale di AstroFisica – Istituto di Astrofisica e Planetologia Spaziali (INAF-IAPS), 00133 Rome, Italy

¹⁵ Jet Propulsion Laboratory, California Institute of Technology, Pasadena, California 91109, USA

Received / Accepted

ABSTRACT

Jupiter's icy moon Ganymede has a tenuous exosphere produced by sputtering and possibly sublimation of water ice. To date, only atomic hydrogen and oxygen have been directly detected in this exosphere. Here, we present observations of Ganymede's CO₂ exosphere obtained with the *James Webb* Space Telescope. CO₂ gas is observed over different terrain types, mainly over those exposed to intense Jovian plasma irradiation, as well as over some bright or dark terrains. Despite warm surface temperatures, the CO₂ abundance over equatorial subsolar regions is low. CO₂ vapor has the highest abundance over the north polar cap of the leading hemisphere, reaching a surface pressure of 1 pbar. From modeling we show that the local enhancement observed near 12 h local time in this region can be explained by the presence of cold traps enabling CO₂ adsorption. However, whether the release mechanism in this high-latitude region is sputtering or sublimation remains unclear. The north polar cap of the leading hemisphere also has unique surface-ice properties, probably linked to the presence of the large atmospheric CO₂ excess over this region. These CO₂ molecules might have been initially released in the atmosphere after the radiolysis of CO₂ precursors, or from the sputtering of CO₂ embedded in the H₂O ice bedrock. Dark terrains (regions), more widespread on the north versus south polar regions, possibly harbor CO₂ precursors. CO₂ molecules would then be redistributed via cold trapping on ice-rich terrains of the polar cap and be diurnally released and redeposited on these terrains. Ganymede's CO₂ exosphere highlights the complexity of surface-atmosphere interactions on Jupiter's icy Galilean moons.

Key words. Planets and satellites: individual: Ganymede, Planets and satellites: atmospheres, Planets and satellites: composition, Infrared: planetary systems

1. Introduction

Jupiter's icy satellites, Europa, Ganymede and Callisto, are known to have rarefied atmospheres. The surface composition of these moons is dominated by H₂O ice and non-ice components (possibly salts, hydrated minerals and organics) that host volatiles such as CO₂ (Carlson et al. 1996; McCord et al. 1998; Tosi et al. 2024). Sublimation and weathering processes, such as sputtering by charged particles from Jupiter's magnetosphere and micro-meteoroid bombardment, lead to the formation of

weakly bound atmospheres composed primarily of H₂O, O₂, OH, H, O, and CO₂ species. Because of strong telluric absorption by Earth's atmosphere, detection of atomic and molecular emissions from icy moon exospheres is difficult from ground-based facilities. Most of our knowledge comes from the detection of auroral O and H emission lines in the atmospheres of the three icy moons (Hall et al. 1998; Cunningham et al. 2015; Barth et al. 1997; Roth et al. 2017a,b; de Kleer et al. 2023), with some constraints obtained on H₂O vapor content for Ganymede (Roth et al. 2021). To date, atmospheric CO₂ has only been de-

20 tected in the atmosphere of Callisto (Carlson 1999; Cartwright
21 et al. 2024). The maximum CO₂ column densities do not co-
22 incide with the subsolar region, nor the regions with the great-
23 est solid-state CO₂ abundance on Callisto’s surface, suggest-
24 ing that CO₂ gas may be partly sourced by outgassing from its
25 crust (Cartwright et al. 2024). Characterizing how icy moon ex-
26 ospheres are formed and sustained is pivotal for understanding
27 surface-atmosphere interactions, geomorphological and chemi-
28 cal changes driven by erosion.

29 Ganymede is the only known moon with an intrinsic mag-
30 netic field, which results in a complex space plasma environ-
31 ment that has been explored by the in situ flybys of the Galileo
32 and Juno spacecraft (e.g., Kivelson et al. 1996; Allegrini et al.
33 2022; Ebert et al. 2022; Clark et al. 2022). The intrinsic mag-
34 netic field directs most of the external Jovian magnetospheric
35 plasma in a way that it primarily interacts with the moon’s sur-
36 face where Ganymede’s mini-magnetosphere has open field lines
37 (i.e., around the polar regions) (Poppe et al. 2018; Liuzzo et al.
38 2020; Greathouse et al. 2022). This results in specific surface
39 properties with respect to shielded equatorial latitudes, such as
40 the formation of H₂O ice-rich patches at the polar caps (Khu-
41 rana et al. 2007; Ligier et al. 2019; Stephan et al. 2020; King
42 & Fletcher 2022) with higher amounts of amorphous H₂O ice
43 (Ligier et al. 2019; Bockelée-Morvan et al. 2024), radiolytically
44 produced H₂O₂ (Trumbo et al. 2023), and CO₂ possibly trapped
45 in amorphous H₂O ice (Bockelée-Morvan et al. 2024). In addi-
46 tion, asymmetries between the north and south polar caps, and
47 leading and trailing hemispheres are observed (Ligier et al. 2019;
48 de Kleer et al. 2021; Trumbo et al. 2023; Bockelée-Morvan et al.
49 2024). Here we present the first detection of CO₂ in the ex-
50 osphere of Ganymede, achieved using the *James Webb* Space
51 Telescope (JWST), and we link the observed highly heteroge-
52 neous CO₂ exosphere to surface properties and processes. This
53 paper follows the investigation of Ganymede’s surface proper-
54 ties from the same JWST data set (Bockelée-Morvan et al. 2024,
55 hereafter Paper I).

56 2. JWST observations of Ganymede’s exosphere

57 Observations undertaken with the Near-Infrared Spectrograph
58 integral field unit (NIRSpec/IFU) provided spatially resolved
59 spectra (0.1” pixel size, with ~190 pixels across Ganymede’s
60 disk) of the leading and trailing sides of Ganymede in the 2.9–5.2
61 μm range at high spectral resolution ($R \sim 3000$) (Paper I and Ap-
62 pendix A). Ro-vibrational emission lines of the CO₂ ν_3 band at
63 4.26 μm were detected within the broad solid-state CO₂ absorp-
64 tion band (Figs 1, B.1). We used several data processing tech-
65 niques to extract the CO₂ gas signal and best evaluate the confi-
66 dence level of the detection for weak signals (Appendices B,
67 C). CO₂ column densities were inferred using a nonlocal ther-
68 mal equilibrium (non-LTE) excitation model (Appendices D, E).
69 The distributions of column densities for the two hemispheres
70 are shown in Fig. 1. Figure 2 presents the dependence on lati-
71 tude, from the analysis of spectra after averaging pixels over
72 ranges of latitude.

73 The distribution of CO₂ gas shows strong regional variations
74 (Fig. 1) and is at odds with expectations that the peak surface
75 location of the exosphere would be at the dawn terminator due
76 to condensation on the surface at night and early morning re-
77 evaporation (Steckloff et al. 2022). The CO₂ exosphere is most
78 prominent over the north polar regions of the leading hemi-
79 sphere, peaking at 81°W, 51°N (12 h local time), with a col-
80 umn density along the line of sight of $(1.5 \pm 0.11) \times 10^{18} \text{ m}^{-2}$
81 corresponding to a pressure at the surface of 1 pbar. The rota-

82 tional temperature of CO₂ measured in this region (107±5 K,
83 Fig. H.1) constrains the gas kinetic temperature in Ganymede’s
84 exosphere (Appendix H). A point-spread function (PSF) correc-
85 tion to the CO₂ column density map suggests that the decrease
86 poleward of 50°N is real (Appendix M). At southern latitudes of
87 the leading hemisphere, and on the trailing hemisphere, the CO₂
88 exosphere is on average at least five times less dense (Fig. 2).
89 Low column densities are measured at or near equatorial lati-
90 tudes for both hemispheres. The trailing hemisphere displays
91 a north–south asymmetry, with the exosphere extending over a
92 broader range of latitudes in the southern hemisphere. Notice-
93 able in Fig. 1 (see also Fig. O.1) is a CO₂ gas enhancement in a
94 large region around (30°W, 25°N), encompassing the Tros crater
95 (27°W, 11°N). CO₂ excess is also present at around 30°S on the
96 leading side, which corresponds to the position of the expected
97 southern open-closed field-line boundary (OCFB, Appendix J).

98 Exospheric H₂O was unsuccessfully searched for in 5.5–7.1
99 μm spectro-imaging data acquired with the JWST Mid-Infrared
100 Instrument (MIRI) Medium Resolution Spectroscopy (MRS)
101 mode (see Appendix I). Our 3σ upper limit on the H₂O column
102 density for the subsolar region of the leading side ($6.8 \times 10^{19} \text{ m}^{-2}$,
103 Table I.1) is about an order of magnitude higher than the mini-
104 mum of $6 \times 10^{18} \text{ m}^{-2}$ required to explain UV Hubble Space Tele-
105 scope (HST) data of atomic oxygen emission lines (Roth et al.
106 2021). On the other hand, for the trailing side, our derived upper
107 limit for a 105 K atmosphere ($3.1 \times 10^{19} \text{ m}^{-2}$) is slightly below
108 the lower limit from HST ($3.6 \times 10^{19} \text{ m}^{-2}$, Roth et al. 2021). Since
109 HST constrains the H₂O/O₂ ratio and not directly the H₂O abun-
110 dance, this could imply that the atmosphere is overall more dilute
111 and that the H₂O and O₂ densities are both lower than assumed
112 in Roth et al. (2021). This would contradict recent results that
113 suggested a denser global atmosphere based on plasma measure-
114 ments (Carnielli et al. 2020a; Waite et al. 2024). Alternatively, a
115 higher atmospheric temperature (e.g., 130 K, Table I.1), as might
116 be expected above subsolar regions, increases the JWST upper
117 limit to values consistent with the HST lower limits.

118 3. Processes releasing CO₂ in Ganymede’s 119 exosphere

120 Possible processes that release CO₂ into Ganymede’s exosphere
121 include surface ice sublimation and sputtering by energetic par-
122 ticles. We investigated whether these mechanisms, acting either
123 on H₂O ice containing CO₂ molecules or on pure CO₂ ice, could
124 be distinguished from the observed properties of Ganymede’s
125 exosphere. For this purpose, we used the Exospheric Global
126 Model Leblanc et al. (EGM, 2017), a multi-species 3D Monte
127 Carlo model that considers sources and sinks (photodestruction,
128 surface sticking, gravitational escape) of such exospheres (Ap-
129 pendix K). The simulations (Appendix L) were designed to ex-
130 plain to first order the CO₂ column density peak observed in the
131 northern latitudes of the leading hemisphere, and the dichotomy
132 between the trailing and leading hemispheres.

133 A key question to address is the localized character of the at-
134 mosphere. Mean surface temperatures, even in the polar regions
135 (100–110 K, Fig. K.1), are much warmer than the expected con-
136 densation temperature of pure CO₂ (73 K at 1 pbar pressure).
137 Hence, the CO₂ atmosphere might have been expected to be
138 more widespread, as shown by EGM calculations considering
139 mean surface temperatures (Appendix L.1). This indicates that
140 CO₂ interacts with the surface material much more strongly than
141 expected in such a simplistic view. Similar conclusions were
142 reached for O₂ gas at Ganymede (Waite et al. 2024), but also

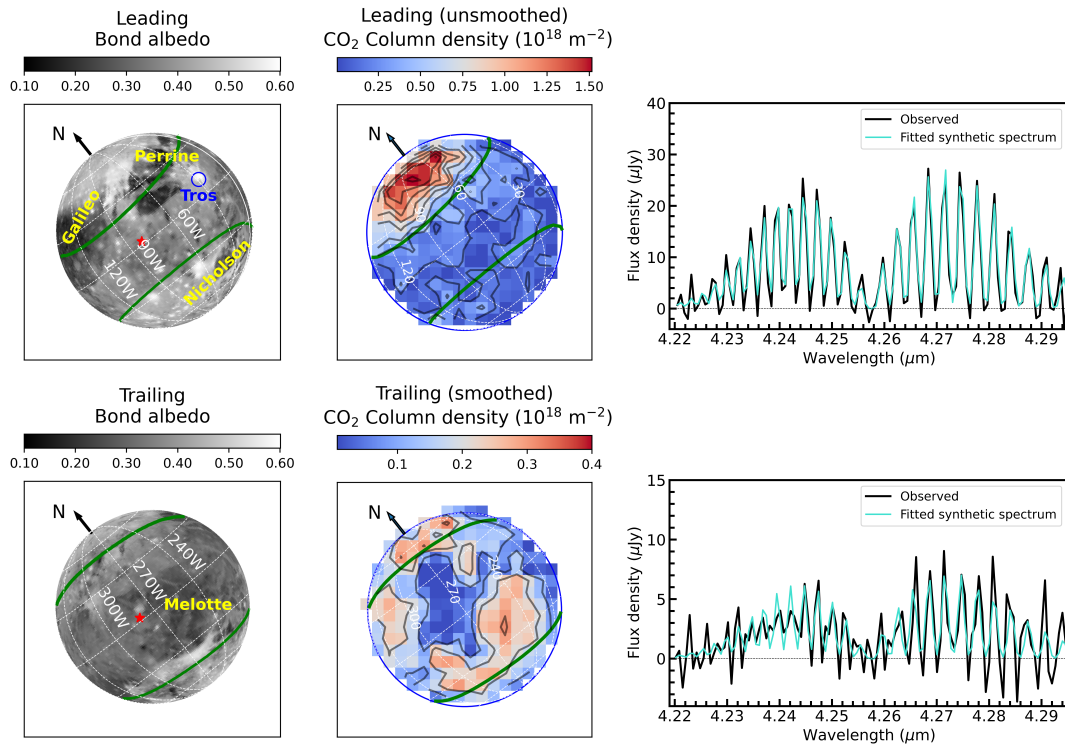


Fig. 1. CO₂ in Ganymede's exosphere. The top and bottom rows are for the leading and trailing sides, respectively. The left column shows Bond albedo maps derived by de Kleer et al. (2021) from Voyager-Galileo mosaic. The middle column shows line-of-sight CO₂ column density maps inferred from spectral modeling (Appendices B–D). The trailing data were smoothed using a 3×3 boxcar filter. The color scales for the leading and trailing sides differ, and are indicated above the plots. The pixel sizes are 0.1×0.1'' and the PSF is ~0.19'' (FWHM). The CO₂ maximal emission in the leading hemisphere (based on central contour) is at 81°W, 51°N (~12h local time); correcting for the line of sight, the maximum vertical column density is at 72°W, 45°N (12.6 h local time, see Figs. 4A, O.2). The third column shows CO₂ gaseous emission spectra obtained after removing the continuum emission from Ganymede's surface, averaged over latitudes 45–90°N for leading (top), and 30–60°S for trailing (bottom). The best fit synthetic spectra are shown in cyan, with a fitted rotational temperature of 108±8 K for the leading side, and a fixed rotational temperature of 105 K for the trailing side. The y scale is μJy per pixel. The green lines on the maps show the OCFBs at the time of the JWST observations (Appendix J, Duling et al. 2022). The subsolar point is shown by a red star in the Bond albedo maps.

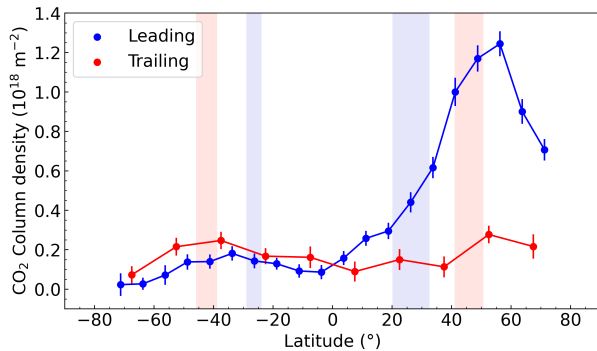


Fig. 2. Variation of CO₂ gas line-of-sight column density with latitude. The blue and red symbols refer to the leading and trailing sides, respectively. The column densities were derived from spectra that were averaged in latitude bins of 7.5° (leading, Fig. B.2) and 15° (trailing). The blue (resp. pink) vertical domains show the latitude range of the OCFBs for the leading and trailing sides, respectively, restricted to longitudes of 10–130° W (leading) and 210–330° W (trailing).

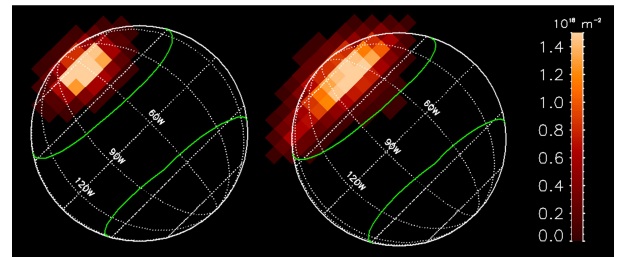


Fig. 3. Calculated line-of-sight column-density maps of the CO₂ exosphere of Ganymede above the leading side from the EGM model (in units of 10¹⁸ m⁻²). Left: CO₂ release associated with H₂O sublimation with a CO₂/H₂O relative abundance of 5 for an H₂O areal ice fraction of 50% at latitudes > 50°N. Right: Sputtering of H₂O ice with CO₂/H₂O = 0.01 at latitudes > 40°N; the result was multiplied by 382 to match the observations (Appendices K, L). The green lines display the OCFBs. The subsolar point is at 2.6°N, 82°W.

at Dione and Rhea (Teolis & Waite 2016), based on inconsis-
 tencies on O₂ column densities between exospheric models and
 measurements. In those moons of Saturn, the O₂ source rates
 implied by the observations are 50 (Dione) to 300 (Rhea) times
 less than expected from the known O₂ radiolysis yields from ion-
 irradiated pure water ice measured in the laboratory, and surface

interactions (adsorption or diffusion) appear to control the exo-
 spheric structure, density, and seasonal variability. We note that
 for CO₂ at Ganymede, the prime evidence for strong surface-
 atmosphere interactions comes from the nonglobal character of
 the atmosphere rather than the absolute CO₂ column densities
 (which remain difficult to explain, see below).

To explain the atmospheric patchiness, Ganymede's surface
 may have properties that increase the effective binding and des-

orption energies of O₂ and CO₂. In addition to surface roughness producing cold traps, surface irradiation (creating defects) and microstructure (enabling diffusion, and re-adsorption on adjacent grains) could increase the effective binding and desorption energies of adsorbates (Yakshinskiy & Madey 2000; Cassidy et al. 2015; Sarantos & Tsavachidis 2020). These hypotheses were drawn to explain the distribution of alkali gases surrounding Mercury and the Moon. In the EGM simulations, the surface temperature model considers surface roughness, as constrained from JWST/MIRI brightness temperature maps (Paper I), and simulates the presence of local cold spots through a temperature distribution (Appendix K). As shown in Appendix L.1, CO₂ diffusion is, to a large extent, controlled by the ability of molecules to condense on cold traps, thereby explaining localized enhancements of the CO₂ exosphere at high latitudes.

Figure 3 shows simulations of Ganymede's CO₂ exosphere above the leading hemisphere, assuming that the release of CO₂ is induced by the sublimation (left panel) or the sputtering (right panel) of H₂O ice containing CO₂ molecules. Sublimation of CO₂ ice was also investigated (Fig. L.2c, d). In all three cases the CO₂ column density peaks at the correct latitude, as long as the source region covers the north polar cap (latitude > 40–50°N, longitude range 0–180°), and follows a diurnal-longitudinal trend with a maximum at ~ 13.1 to 13.4 h, slightly shifted from the maximum surface temperature (12.5 h, Fig. K.1) and observed CO₂ peak (12 h). Sputtering explains the smooth diurnal variation of the CO₂ column density better than sublimation (Fig. L.2f).

In our models where CO₂ is released through sputtering of H₂O ice with 1% CO₂ molecules, we had to multiply the sputtered flux from Leblanc et al. (2017) by a factor of ~ 380 to match the observed peak column density. The need to increase the sputtered flux significantly might be related to the approach used by Leblanc et al. (2017) to calculate this flux (see Appendix K), which consisted in using the yield definition of Cassidy et al. (2013) and a precipitating Jovian ion flux of 10⁶ particles/cm²/s, ignoring any sputtered component from electron impact. Carnielli et al. (2020a) modeled the ion population in the ionosphere and concluded, based on electron measurements from the Galileo spacecraft, that ionospheric ions could be a significant source of ion precipitation, especially on the leading hemisphere (Carnielli et al. 2020b). Using measurements from the Juno spacecraft, Waite et al. (2024) and Vorburger et al. (2024) concluded that low-energy electrons are an important sputtering agent. Another source of uncertainty is sputtering yields for production of CO₂ by ion and electron impacts, which are unconstrained because the relevant experiments are sparse. Simulations investigating sputtering on the entire surface of Ganymede (Appendix L.4) show that it might be possible to explain the overall distribution of CO₂ exosphere by considering strong regional variations of surface properties.

A consequence of the factor of 380 enhancement of the sputtered flux from Leblanc et al. (2017) is that to first order the O₂ column density in our model is multiplied by the same factor, bringing it to values ~ 1.5×10¹⁷ O₂/cm², at odds with results from Leblanc et al. (2023) and Roth et al. (2021), based on the atomic O line intensities in the UV. This result goes in the same direction as the ionospheric calculations of Carnielli et al. (2020b) and the post-Juno analyses of Vorburger et al. (2024) and Waite et al. (2024), who advocated for O₂ columns that are ~20 times enhanced compared to previous estimates, but the discrepancy is much larger here, which at face value could be taken as an argument against sputtering being at the origin of the CO₂ atmosphere.

In our sublimation models where CO₂ gas is released in proportion to the H₂O sublimation flux, reproducing the peak column density requires an unrealistic CO₂ abundance relative to water, three orders of magnitude higher than estimated for the surface (~1% in mass, Paper I). Hence, this scenario cannot explain the CO₂ exospheric excess on the northern polar cap of the leading side. On the other hand, direct sublimation of CO₂ ice is a possible mechanism as only a very small amount of surface coverage (3×10^{-14} , Table L.1) is required to explain the peak column density, albeit with an expected diurnal variation more extreme than observed (Fig. L.2d). Regarding the subsolar regions and considering H₂O ice sublimation with an areal H₂O abundance of 20% appropriate for the leading side (Ligier et al. 2019), our model predicts a H₂O column density of 4.1×10¹⁹ m⁻², consistent with the JWST upper limit for Ganymede's leading hemisphere (Table I.1), but a factor of 7 above the minimum value derived from HST data for this hemisphere (6×10¹⁸ m⁻², Roth et al. 2021).

In summary, the processes that release CO₂ in Ganymede's exosphere are not well understood. The smooth diurnal variation of the CO₂ column density favors sputtering, but explaining the measured column densities with this process requires further model developments that take advantage of the most recent magnetospheric data acquired by the Juno mission. We can anticipate that the interpretation of Callisto's CO₂ exosphere (Cartwright et al. 2024), which is one order of magnitude denser than Ganymede's CO₂ exosphere, will be similarly challenging.

4. Linking Ganymede's CO₂ exosphere to surface properties

The 4.26 μm absorption band of surface CO₂ is ubiquitous on Ganymede, and is caused by CO₂ under different physical states. However, the CO₂ gas column density does not correlate with the CO₂ surface distribution globally (Fig. 4A, B; see Appendix N and Figs N.1A, C, D, F). Rather, the prominence of the CO₂ exosphere on the northern polar cap is associated with other surface properties.

According to Galileo high-resolution images, Ganymede's polar caps are actually made of discrete patches of optically thick ice, preferentially located on pole-facing slopes (Khurana et al. 2007), likely formed by H₂O ice sputtering and subsequent re-deposition on these coldest locations (Khurana et al. 2007). On both hemispheres, Ganymede's north polar regions show spectral properties indicative of H₂O ice particles having a higher density of facets for the photons (i.e., smaller grains and/or more internal defects and/or higher micro-roughness/porosity) causing multiple scattering and a higher proportion of amorphous ice than the south polar regions (Denk et al. 2009; Ligier et al. 2019, Paper I) (Fig. 4D,E,F).

Remarkably, these north-south polar asymmetries in spectral properties are most pronounced on the leading hemisphere. As shown in Fig. 4, the fact that the peak column density of CO₂ gas is found over regions where water ice has the highest density of facets, the largest amorphous fraction, and the most red-shifted absorption band center of solid CO₂ (indicative of CO₂ trapped in amorphous H₂O ice) suggests that all these properties are probably linked. They are co-located poleward of 40°N, so they are probably specific to the ice-rich patches constituting the polar cap. The CO₂ exosphere is maximum over the polar cap, but it extends over all of the northern open field-lines area.

During the JWST observation of the leading side, the southern hemisphere of Ganymede was facing toward the center of

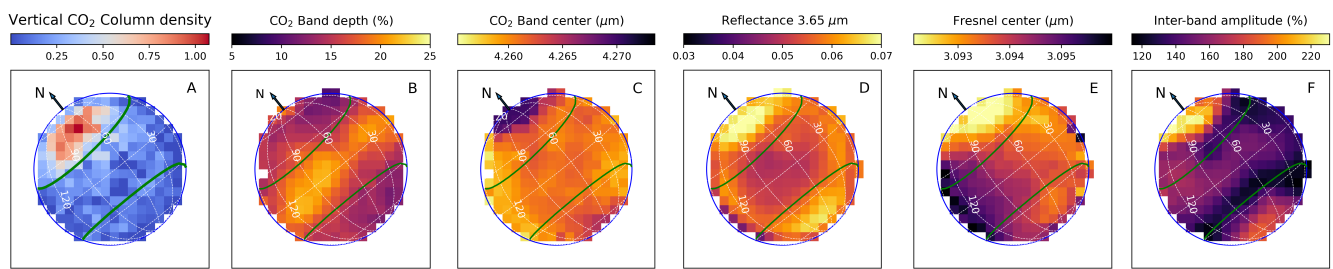


Fig. 4. Comparing CO₂ exosphere to surface properties on Ganymede's leading hemisphere. A) Vertical CO₂ gas column density (in units of 10¹⁸ m⁻², this work, see also Fig. O.2); B) Depth of CO₂-solid absorption band (Paper I); C) Central wavelength of CO₂-solid absorption band (Paper I); D) Reflectance at 3.65 μm (Paper I); E) Central wavelength of H₂O Fresnel peak (Paper I); F) Relative amplitude of the maximum reflectance between 3.5 and 4 μm (H₂O interband amplitude, Paper I). The north pole of the leading hemisphere possesses the most redshifted absorption band center of solid CO₂, consistent with CO₂ trapped in amorphous H₂O ice (Paper I). It also has the highest reflectance at 3.65 μm and H₂O interband amplitude, indicative of a higher density of facets in H₂O ice for the photons (i.e., smaller grains and/or more internal defects and/or higher micro-roughness or porosity), and the most blueshifted central wavelength of the H₂O Fresnel peak due to a higher proportion of amorphous water ice (Mastrapa et al. 2009).

the plasma sheet, where the column density of plasma along Jupiter's magnetospheric field lines is higher than on the northern side of the plasma sheet. On the plasma sheet facing hemisphere, the auroral band of Ganymede is brighter than on the other hemisphere (Saur et al. 2022; Greathouse et al. 2022; Milby et al. 2024). The reason for the auroral asymmetry is not fully understood. It could be due to the greater plasma momentum and resultant greater magnetic stresses on hemispheres facing the plasma sheet center and/or asymmetric reconnection processes (e.g., Saur et al. 2022; Milby et al. 2024). The higher auroral brightness requires higher auroral electron fluxes of which the largest fraction will collide with the surface. Additionally, the hemisphere facing the center of the plasma sheet is facing higher fluxes of energetic ions and electrons. Integrating these electron and ion fluxes over a full Jovian synodic rotation period should however lead to similar fluxes on the northern and southern polar regions (Poppe et al. 2018; Liuzzo et al. 2020). The observations of higher density of CO₂ gas and of enhanced/specific surface properties on the northern hemisphere of the leading side are thus not consistent with what would be expected from either instantaneous or time-averaged plasma effects. Therefore, the specifics of the north polar regions of the leading hemisphere are likely an inherent property of Ganymede's surface.

The north and south polar caps mainly differ in the nature of their underlying terrains. Galileo Regio, the largest patch of the darker and more cratered terrains on Ganymede, encompasses much of the leading north polar latitudes, while the leading south polar latitudes have fewer of these dark cratered terrains (Fig. O.3 from Paterson et al. (2010)). The low-albedo material, concentrated in topographic lows by sublimation and mass wasting (Prockter et al. 1998), may be a remnant of Ganymede's formation building blocks and/or may have been deposited by comet-like bodies (Zahnle et al. 1998; Bottke et al. 2013), so it could contain CO₂ precursors (organic and inorganic carbon-bearing components), whose radiolysis and/or disaggregation by energetic particles may produce and/or release CO₂. As shown by laboratory experiments, the radiolysis of complex organic matter (Gomis & Strazzulla 2005; Raut et al. 2012) or carbonates (Costagliola et al. 2017) in the presence of H₂O forms CO₂. In addition, the disaggregation of carbonaceous chondrite-like material (Yuen et al. 1984) or the radiolysis of some of their inorganic carbon-bearing components (carbonates and other minerals, Nakamura et al. 2023) could also release or produce CO₂. This CO₂ production may be specifically enhanced in the northern open field-lines area of the leading hemisphere because they

host the largest extent of dark cratered terrains than the southern ones (Fig. O.3).

However, the peak in CO₂ column density is not only over the fraction of Galileo Regio poleward of the OCFB, but over the water ice polar cap (Fig. 4A, D, F; Fig. N.1B), covering diverse terrain types (Fig. 1). Moreover, the peak of the CO₂ vertical column density is at 72°W, 45°N (12.6 h local time), on the boundary between Galileo Regio and the bright terrain Xibalba Sulcus (Fig. 1, Fig. O.3). Therefore, if the CO₂ is initially produced on the dark terrains, it should migrate and accumulate over the polar cap on the long term, before being diurnally released and redeposited over the polar cap as is possibly observed. This redistribution might also occur if the CO₂ is initially produced from other sources, for example by a relatively recent resurfacing event (impact, mass movement) that would have exposed to the surface CO₂ or CO₂ precursors originating from the sub-surface and/or from the impactor. Notably, several impact craters with bright ejecta are present over the part of Xibalba Sulcus showing maximum CO₂ column density (Collins et al. 2014), and the ice bedrock of this relatively recent region is thought to contain significant CO₂ based on its geomorphology (Moore et al. 1999). If this CO₂ exosphere is permanent, geological mass-wasting events (Moore et al. 1999; Pappalardo et al. 2004) and possibly micrometeoritic gardening, may regularly expose new CO₂ or CO₂ precursors to the surface, maintaining the CO₂ exosphere over the long-term. The release of CO₂ gas from ongoing volcanic activity seems unlikely given the surface age (0.5–1 Ga with large uncertainties, Zahnle et al. 1998; Showman et al. 2004), but gravity anomalies were identified around this region (Gomez Casajus et al. 2022).

The produced CO₂ may then preferentially co-deposit with H₂O and accumulate on high-latitude cold traps, which potentially explains the redshift of the CO₂ absorption band with latitude (Fig. 4C). The maximum CO₂ column densities and the H₂O ice having the highest density of facets both peak around a longitude at the maximum solar illumination and maximum surface temperature at this latitude (Paper I), suggesting a diurnal process that releases CO₂ from the ice in the atmosphere (Fig. 4A, D, F). According to our analyses, sputtering appears to have a temperature dependence that is the most consistent with the observation (Fig. L.2). At mid-day, the maximum temperature of the ice enhances sputtering and thermal stress that may generate more ice facets, resulting in surface micro-roughness or internal cracks, which could further enhance CO₂ release (Baragiola 2003, and references therein). Later in the day and night,

372 re-deposition and/or molecular movements induced by energetic
373 ions might fill in these pores or cracks, decreasing the density of
374 facets and trapping the CO₂ again.

375 5. Summary

376 In summary, the north-south polar asymmetry in the distribution
377 of CO₂ gas of the leading hemisphere could be explained by the
378 larger extent of dark terrains over the northern polar region, pro-
379 viding a larger initial source of CO₂ produced by radiolysis of
380 organic or inorganic precursors. The existence of other initial
381 sources specific to this region (impact, mass movement, cryo-
382 volcanism) cannot be excluded, but there is a lack of compelling
383 evidence. After its initial production, CO₂ may migrate and ac-
384 cumulate on cold traps of the polar cap and be diurnally released
385 and redeposited, explaining the co-location of the northern polar
386 atmosphere with the H₂O and CO₂ surface properties. Whether
387 the release mechanism in this high-latitude region is sputtering
388 or sublimation remains unclear. Outside of the open field-line
389 areas, CO₂ gas is located above various terrain types, including
390 the dark terrain Melotte and some other terrains having more (or
391 smaller) grains of H₂O ice or H₂O-bearing minerals and/or salts
392 (Fig. N.1B, E). This spatial distribution suggests the existence of
393 several mechanisms producing and releasing CO₂. Future inves-
394 tigations of Ganymede from JWST and space missions, together
395 with further models and experiments dedicated to sputtering pro-
396 cesses, are needed to unravel the origin of Ganymede's patchy
397 CO₂ exosphere.

398 *Acknowledgements.* This work is based on observations made with the
399 NASA/ESA/CSA *James Webb* Space Telescope. The data were obtained from
400 the Mikulski Archive for Space Telescopes at the Space Telescope Science Insti-
401 tute, which is operated by the Association of Universities for Research in Astron-
402 omy, Inc., under NASA contract NAS 5-03127 for JWST. These observations are
403 associated with program 1373, which is led by co-PIs Imke de Pater and Thierry
404 Fouchet and has a zero-exclusive-access period. D.B.-M, E.Q., E.L., T.F., and
405 O.P. acknowledge support from the French Agence Nationale de la Recherche
406 (program PRESSE, ANR-21-CE49-0020-01). I.dP and M.H.W. were in part sup-
407 ported by the Space Telescope Science Institute grant nr. JWST-ERS-01373. L.F.
408 was supported by STFC Consolidated Grant reference ST/W00089X/1; for the
409 purpose of open access, the author has applied a Creative Commons Attribution
410 (CC BY) licence to the Author Accepted Manuscript version arising from this
411 submission. Some of this research was carried out at the Jet Propulsion Labo-
412 ratory, California Institute of Technology, under a contract with the National
413 Aeronautics and Space Administration (80NM0018D0004).

414 References

415 Allegrini, F., Bagenal, F., Ebert, R. W., et al. 2022, *Geophys. Res. Lett.*, 49,
416 e2022GL098682
417 Baragiola, R. A. 2003, *P&SS*, 51, 953
418 Barth, C. A., Hord, C. W., Stewart, A. I. F., et al. 1997, *Geophys. Res. Lett.*, 24,
419 2147
420 Blauer, J. & Nickerson, G. 1973, GA survey of vibrational relaxation rate data
421 for processes important to CO₂-N₂-H₂O infrared plume radiation, Tech. rep.,
422 U.S. Geological Survey, technical Report AFRPL-TR-73- 57 Ultrasytems,
423 Inc.
424 Bockelée-Morvan, D., Lellouch, E., Poch, O., et al. 2024, *A&A*, 681, A27 (Paper
425 I)
426 Bottke, W. F., Vokrouhlický, D., Nesvorný, D., & Moore, J. M. 2013, *Icarus*,
427 223, 775
428 Carlson, R., Smythe, W., Baines, K., et al. 1996, *Science*, 274, 385
429 Carlson, R. W. 1999, *Science*, 283, 820
430 Carnielli, G., Galand, M., Leblanc, F., et al. 2020a, *Icarus*, 343, 113691
431 Carnielli, G., Galand, M., Leblanc, F., et al. 2020b, *Icarus*, 351, 113918
432 Cartwright, R. J., Villanueva, G. L., Holler, B. J., et al. 2024, *PSJ*, 5, 60
433 Cassidy, T. A., Merkel, A. W., Burger, M. H., et al. 2015, *Icarus*, 248, 547
434 Cassidy, T. A., Paranicas, C. P., Shirley, J. H., et al. 2013, *P&SS*, 77, 64
435 Clark, G., Kollmann, P., Mauk, B. H., et al. 2022, *Geophys. Res. Lett.*, 49,
436 e2022GL098572

Collins, G. C., Patterson, G. W., Head, J. W., et al. 2014, Global geologic map
of Ganymede, Tech. Rep. 3237, U.S. Geological Survey, iSSN: 2329-132X
Publication Title: Scientific Investigations Map
Costagliola, A., Vandenborre, J., Blain, G., et al. 2017, *The Journal of Physical
Chemistry C*, 121, 24548, publisher: American Chemical Society
Crovissier, J. 1987, *A&A Suppl.*, 68, 223
Cunningham, N. J., Spencer, J. R., Feldman, P. D., et al. 2015, *Icarus*, 254, 178
Davidsson, B. J. R. & Hosseini, S. 2021, *MNRAS*, 506, 3421
de Kleer, K., Butler, B., de Pater, I., et al. 2021, *PSJ*, 2, 5
de Kleer, K., Milby, Z., Schmidt, C., Camarca, M., & Brown, M. E. 2023, *PSJ*,
4, 37
Denk, T., Neukum, G., Khurana, K. K., & Pappalardo, R. T. 2009, in *EPSC 2009*,
572
Duling, S., Saur, J., Clark, G., et al. 2022, *GRL*, 49, e2022GL101688
Ebert, R. W., Fuselier, S. A., Allegrini, F., et al. 2022, *Geophys. Res. Lett.*, 49,
e2022GL099775
Famá, M., Shi, J., & Baragiola, R. A. 2008, *Surface Science*, 602, 156
Fray, N. & Schmitt, B. 2009, *P&SS*, 57, 2053
Gomez Casajus, L., Ermakov, A. I., Zannoni, M., et al. 2022, *Geophys. Res.
Lett.*, 49, e2022GL099475
Gomis, O. & Strazzulla, G. 2005, *Icarus*, 177, 570
Gordon, I. E., Rothman, L. S., Hargreaves, R. J., et al. 2022, *JQRST*, 277, 107949
Greathouse, T. K., Gladstone, G. R., Molyneux, P. M., et al. 2022, *GRL*, 49,
e2022GL099794
Hall, D. T., Feldman, P. D., McGrath, M. A., & Strobel, D. F. 1998, *The Astro-
physics Journal*, 499, 475
Hapke, B. 1984, *Icarus*, 59, 41
Hase, F., Wallace, L., McLeod, S. D., Harrison, J. J., & Bernath, P. F. 2010,
JQRST, 111, 521
Hayne, P. O., Aharonson, O., & Schörghofer, N. 2021, *Nature Astronomy*, 5, 169
Hibbitts, C. A., McCord, T. B., & Hansen, G. B. 2000, *JGR: Planets*, 105, 22541
Hibbitts, C. A., Pappalardo, R. T., Hansen, G. B., & McCord, T. B. 2003, *JGR
(Planets)*, 108, 5036
Hom, E. F. Y., Marchis, F., Lee, T. K., et al. 2007, *Journal of the Optical Society
of America A*, 24, 1580
Itikawa, Y. 2002, *Journal of Physical and Chemical Reference Data*, 31, 749
Khurana, K. K., Pappalardo, R. T., Murphy, N., & Denk, T. 2007, *Icarus*, 191,
193
King, O. & Fletcher, L. N. 2022, *JGR: Planets*, 127, e2022JE007323
Kivelson, M. G., Khurana, K. K., Russell, C. T., et al. 1996, *Nature*, 384, 537
Leblanc, F., Oza, A. V., Leclercq, L., et al. 2017, *Icarus*, 293, 185
Leblanc, F., Roth, L., Chaufray, J. Y., et al. 2023, *Icarus*, 399, 115557
Ligier, N., Paranicas, C., Carter, J., et al. 2019, *Icarus*, 333, 496
Liuzzo, L., Poppe, A. R., Paranicas, C., et al. 2020, *JGR: Space Physics*, 125,
e2020JA028347
Málin, M., Boccaletti, A., Charnay, B., Kiefer, F., & Bézard, B. 2023, *A&A*,
671, A109
Mastrapa, R. M., Sandford, S. A., Roush, T. L., Cruikshank, D. P., & Dalle Ore,
C. M. 2009, *ApJ*, 701, 1347
McCord, T. B., Hansen, G. B., Clark, R. N., et al. 1998, *JGR: Planets*, 103, 8603
Milby, Z., de Kleer, K., Schmidt, C., & Leblanc, F. 2024, *PSJ*, 5, 153
Moore, J. M., Asphaug, E., Morrison, D., et al. 1999, *Icarus*, 140, 294
Nakamura, T., Matsumoto, M., Amano, K., et al. 2023, *Science*, 379, abn8671
Pappalardo, R. T., Collins, G. C., Head, James W., I., et al. 2004, in *Jupiter. The
Planet, Satellites and Magnetosphere*, ed. F. Bagenal, T. E. Dowling, & W. B.
McKinnon, Vol. 1 (Cambridge University Press), 363–396
Patterson, G. W., Collins, G. C., Head, J. W., et al. 2010, *Icarus*, 207, 845
Poppe, A. R., Fatemi, S., & Khurana, K. K. 2018, *JGR: Space Physics*, 123, 4614
Prockter, L. M., Head, J. W., Pappalardo, R. T., et al. 1998, *Icarus*, 135, 317
Raut, U., Fulvio, D., Loeffler, M. J., & Baragiola, R. A. 2012, *ApJ*, 752, 159,
publisher: The American Astronomical Society
Roth, L., Alday, J., Becker, T. M., Ivchenko, N., & Retherford, K. D. 2017a, *JGR
(Planets)*, 122, 1046
Roth, L., Ivchenko, N., Gladstone, G. R., et al. 2021, *Nature Astronomy*, 5, 1043
Roth, L., Retherford, K. D., Ivchenko, N., et al. 2017b, *AJ*, 153, 67
Sandford, S. & Allamandola, L. 1990, *ApJ*, 355, 357
Santos, M. & Tsavachidis, S. 2020, *Geophys. Res. Lett.*, 47, e88930
Saur, J., Duling, S., Roth, L., et al. 2015, *JGR (Space Physics)*, 120, 1715
Saur, J., Duling, S., Wennmacher, A., et al. 2022, *Geophys. Res. Lett.*, 49,
e2022GL098600
Showman, A. P., Mosqueira, I., & Head, J. W. 2004, *Icarus*, 172, 625
Snellen, I. A. G., de Kok, R. J., de Mooij, E. J. W., & Albrecht, S. 2010, *Nature*,
465, 1049
Steckloff, J. K., Goldstein, D., Trafton, L., Varghese, P., & Prem, P. 2022, *Icarus*,
384, 115092
Stephan, K., Hibbitts, C. A., & Jaumann, R. 2020, *Icarus*, 337, 113440
Teolis, B. D., Plainaki, C., Cassidy, T. A., & Raut, U. 2017, *JGR (Planets)*, 122,
1996
Teolis, B. D. & Waite, J. H. 2016, *Icarus*, 272, 277
Tosi, F., Mura, A., Cofano, A., et al. 2024, *Nature Astronomy*, 8, 82
Trumbo, S. K., Brown, M. E., Bockelée-Morvan, D., et al. 2023, *Science Ad-
vances*, 9, eadg3724
Villanueva, G. L., Smith, M. D., Protopapa, S., Faggi, S., & Mandell, A. M.
2018, *JQRST*, 217, 86
Vorburger, A., Fatemi, S., Carberry Mogan, S. R., et al. 2024, *Icarus*, 409, 115847
Waite, J. H., Greathouse, T. K., Carberry Mogan, S. R., et al. 2024, *JGR (Plan-
ets)*, 129, e2023JE007859
Yakshinskiy, B. V. & Madey, T. E. 2000, *Surface Science*, 451, 160
Yuen, G., Blair, N., Marais, D. J. D., & Chang, S. 1984, *Nature*, 307, 252
Zahnle, K., Dones, L., & Levison, H. F. 1998, *Icarus*, 136, 202

527 **Appendix A: JWST observations and data reduction**

528 NIRSspec/IFU observations of the leading and trailing sides of
 529 Ganymede were obtained as part of the Early Release Science
 530 (ERS) program #1373 (PIs I. de Pater, T. Fouchet). These obser-
 531 vations, acquired with the G395H/F290LP grating/filter pair,
 532 provided spatially resolved imaging spectroscopy in the range
 533 2.86–5.28 μm over a 3'' \times 3'' field of view with 0.1'' \times 0.1'' spatial
 534 elements (310 \times 310 km at Ganymede), and a nominal spec-
 535 tral resolution of $R \sim 2700$. The estimated full width at half
 536 maximum of the point spread function (PSF) is $\sim 0.19''$ (Ap-
 537 pendix M). Detailed information on these observations is pro-
 538 vided in Trumbo et al. (2023) and Paper I, focused on the analy-
 539 sis of solid state spectral features from CO₂, H₂O, and H₂O₂.
 540 For the data reduction we followed the procedure adopted in
 541 Bockelée-Morvan et al. (2024) (Paper I). The updated JWST
 542 pipeline version 1.12.5 and context file version *jwst_1148.pmap*
 543 were used. Correction for the 1/f noise was done as explained in
 544 Trumbo et al. (2023) and Paper I.

545 ERS #1373 comprised also observations of the leading and
 546 trailing sides of Ganymede using the Mid-Infrared Instru-
 547 ment/medium resolution spectroscopy (MIRI/MRS), which are
 548 described in Paper I. These observations, made with the four IFU
 549 channels, provided spatially-resolved unsaturated spectra in the
 550 4.9–11.7 μm range. Channel 1 (4.9–7.65 μm) covers the ν_2 vi-
 551 brational band (and weaker $\nu_2+\nu_3-\nu_3$ and $\nu_2+\nu_1-\nu_1$ hot-bands)
 552 of H₂O in vapor phase from which the H₂O content in Ganymede's
 553 exosphere can be studied. For Channel 1, the spaxel (aka pixel
 554 in main text) size is 0.13'' and the spectral resolution is ~ 3700 .
 555 The data were re-reduced using most recent JWST pipeline ver-
 556 sion 1.11.3, and context file *jwst_1119.pmap*, and processed as
 557 in Paper I.

558 Ganymede spectra are crowded with solar lines. For the
 559 study of solid-state features in NIRSspec spectra, the output of
 560 the JWST pipeline, calibrated in radiance units (MJy/sr), were
 561 divided by the solar spectrum (Hase et al. 2010) at the spectral
 562 resolution of NIRSspec, giving data in units of radiance factor
 563 I/F (Paper I). To obtain spectra in radiance units and corrected
 564 from solar lines, the data in I/F units were multiplied by the so-
 565 lar continuum. In the spectral 4.2–4.3 μm region where strong
 566 ro-vibrational lines of the CO₂ ν_3 band are present, solar lines
 567 are not numerous and much fainter than in nearby spectral re-
 568 gions. Nevertheless, we payed special attention to solar-line re-
 569 moval as gaseous emission lines from Ganymede are faint. We
 570 determined that solar lines present in the 4.4–4.6 μm range are
 571 best removed when applying a correction factor of ~ 0.87 to the
 572 nominal spectral dispersion provided by JWST documentation
 573 (i.e., increasing the wavelength-dependent spectral resolution by
 574 1.15). We used this factor (giving $R = 3365$ at 4.2–4.3 μm) in
 575 subsequent analyses, including for producing synthetic line pro-
 576 files.

577 In MIRI spectra, the most intense ro-vibrational lines from
 578 the H₂O ν_2 band are expected between 5.6 and 7.4 μm (Fig. I.1).
 579 In this spectral region, both reflected light and thermal emis-
 580 sion from Ganymede's surface contribute to the continuum, es-
 581 pecially at the lowest wavelengths where the two components
 582 have similar intensities (Paper I). Therefore, spectra were cor-
 583 rected from solar lines by isolating the reflected-light compo-
 584 nent, and applying the method used for NIRSspec data.

585 **Appendix B: Extraction of CO₂ gaseous lines**

586 The ν_3 bands of CO₂ in gaseous form and in solid state lie at
 587 the same wavelengths. The solid-state absorption band of CO₂

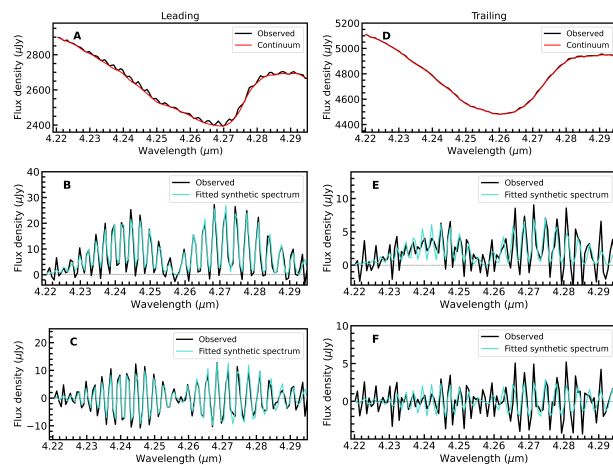


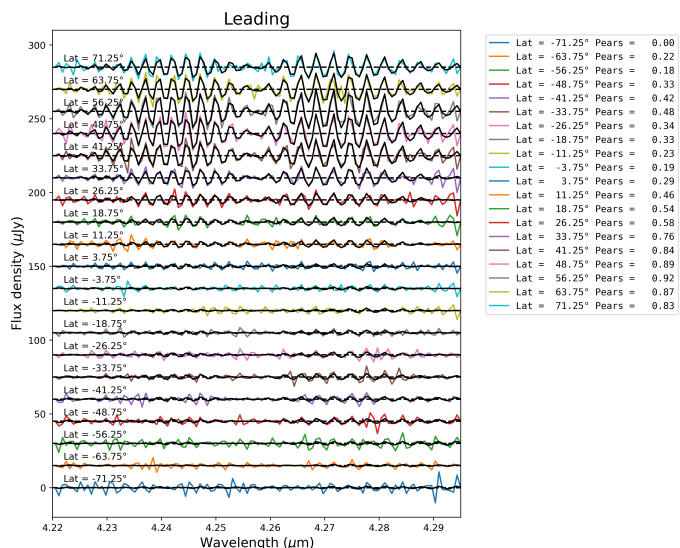
Fig. B.1. CO₂ ν_3 band gas spectra from Ganymede's exosphere. Left (A–C): North polar cap of the leading side of Ganymede (averaged spectra for latitudes $> 45^\circ$ N); Right (D–F): Southern hemisphere of the trailing side (latitudes $30\text{--}60^\circ$ S). A, D) Observed spectra showing both the CO₂ ν_3 absorption band from CO₂ in solid state, and ro-vibrational emission lines of gaseous CO₂; B, E) CO₂ gaseous emission spectra obtained after removing the continuum emission shown in red in panels A and D (Appendix B). C, F) Residual CO₂-gas DIFF spectra obtained by removing the continuum obtained from low-pass filtering (Appendix B). Best fit synthetic spectra are shown in blue, with a fitted rotational temperature of 108 ± 8 K for the leading side, and a fixed rotational temperature of 105 K for the trailing side. In all plots, vertical-axis unit is μJy per pixel (1 pixel = $0.1'' \times 0.1''$).

588 shows strong variations in shape and intensity on the surface of
 589 Ganymede (Paper I). Hence, to isolate the weak ro-vibrational
 590 emission lines from CO₂ gas from the broad absorption band, we
 591 developed specific tools, which were tested on synthetic spectra.
 592 We restricted the analysis to the 4.220–4.295 μm range where
 593 the strongest CO₂ gaseous lines and only weak solar lines are
 594 present.

595 In a first step, the solid-state contribution was estimated by
 596 applying low-pass filtering with a Butterworth filter. The opti-
 597 mum cutoff frequency that preserves best the gaseous signatures
 598 was determined by applying the method to synthetic spectra
 599 combining the Ganymede CO₂-solid absorption band and CO₂-
 600 gas fluorescence emission. In a second step, the residual CO₂
 601 gas signature (called DIFF) was obtained by subtracting this es-
 602 timated solid-state signal from the observed spectra. Two exam-
 603 ples of residual DIFF spectra are shown in Figs B.1C, F. This
 604 method does not allow retrieval of the correct shape of the CO₂
 605 gaseous band. We show in Figs B.1B, E (and Fig. 1) CO₂ gas
 606 spectra from Ganymede displaying the expected ro-vibrational
 607 structure of the CO₂ ν_3 band for fluorescence emission. They
 608 were obtained through several iterations, by computing the en-
 609 velope of the residual DIFF signal and adding the bottom part
 610 of the envelope to the solid-state signal extracted from low-pass
 611 filtering. From synthetic spectra processed in the same manner,
 612 we found that this third step produced an overestimation of the
 613 strength of the CO₂ gas signature, especially for faint signals at
 614 the limit of noise. Hence, analyses were made on DIFF spectra.

615 In order to evaluate the significance of detection of gas
 616 emissions, we computed the Pearson correlation coefficient C_p
 617 between the DIFF spectra and a forward model. The forward
 618 model consists in a DIFF spectrum computed by applying the
 619 same treatment as for the data to a synthetic spectrum obtained
 620 by combining the Ganymede average CO₂ absorption band ob-
 621 served on the leading side (obtained from low-pass filtering)

622 and a CO₂ fluorescence spectrum at 105 K convolved to the
623 instrumental spectral resolution $R = 3365$. The Pearson correla-
624 tion coefficient C_p was computed for each individual spaxel
625 on the leading side. Due to the faintness of the CO₂ gas emis-
626 sion lines on the trailing side, the trailing data were smoothed
627 using a 3×3 boxcar filter. C_p ranges from -0.22 to 0.87 on the
628 leading side, and from -0.11 to 0.50 on the trailing side (left panels
629 of Fig. O.1). Except for the northern regions of the leading
630 Ganymede disk, C_p values do not exceed 0.5 . Hence the confi-
631 dence level of the detection of the CO₂ exosphere is rather low
632 for several regions, calling for the use of other detection criteria
633 (cross-correlation technique).

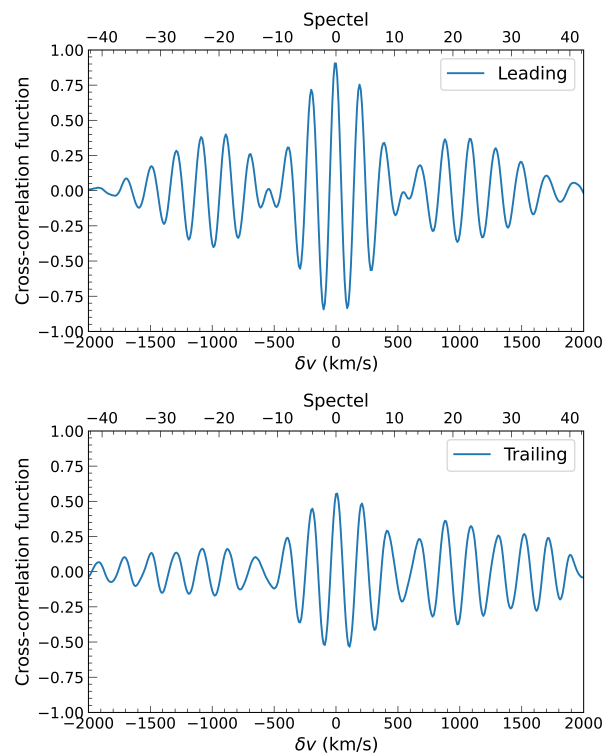


634 **Fig. B.2.** DIFF spectra on the leading hemisphere as a function of latitude. Data were averaged over latitude bins of 7.5° and treated as explained in Appendix B. Fitted fluorescence DIFF spectra are shown in black. The Pearson correlation coefficient for each spectrum is given in the legend. Vertical-axis unit is the flux density per pixel.

634 Appendix C: Cross-correlation technique

635 We used the cross-correlation technique to obtain additional criteria
636 for confirming weak CO₂ detections. This method is widely
637 used, for example to search for molecular signatures in exoplanet
638 spectra (Snellen et al. 2010; Málin et al. 2023). We computed the
639 cross-correlation function (CCF) between the Ganymede DIFF
640 spectra and the forward model over a velocity range (-3000 ,
641 3000) km/s (in total 127 spectral resolution elements, aka spec-
642 trels) using velocity steps δv spaced by 10 km/s (0.21 spectels).
643 Cross-correlating the forward model with itself, the maximum
644 of the autocorrelation function is obviously at $\delta v = 0$. Because
645 of the periodicity in frequency of the CO₂ ro-vibrational lines,
646 which are equally spaced every $0.003 \mu\text{m}$ (~ 4 spectels), the au-
647 tocorrelation function and CCFs present strong secondary peaks
648 (reaching 80 % of the maximum for the closest secondary peaks)
649 spaced by the corresponding value in velocity units (Fig. C.1).
650 The criterion used for confident CO₂ exosphere detection is that
651 the maximum of the CCF stands close to $\delta v = 0$, namely is
652 shifted by at most one spectel element.

653 We estimated the signal-to-noise ratio (S/N_{CCF}) of the CCF
654 at $\delta v = 0$ to quantitatively measure the confidence level of the de-
655 tectations. For that purpose, we generated synthetic spectra adding
656 random Gaussian noise to the Ganymede average CO₂ absorp-
657 tion band observed on the leading side obtained from low-pass



658 **Fig. C.1.** Cross-correlation functions (CCFs). Top: from averaged data
659 at latitudes $> 45^\circ\text{N}$ on the leading hemisphere. Bottom: from averaged
660 data at latitudes $30\text{--}60^\circ\text{S}$ on the trailing hemisphere. The forward model
661 for computing the cross-correlation is a fluorescence CO₂ spectrum. In
662 both cases the CCF peaks at $\delta v = 0$, indicating CO₂ exosphere detection.
663 The maximum of the CCF is lower for the trailing side due to a fainter
664 CO₂ signal.

658 filtering. As there is no possibility of estimating the noise level
659 from the acquired spectra themselves (noise-like features are
660 dominated by residuals in solar lines subtraction), we used the
661 error cube given in the Level 3 hyperspectral data cubes to set the
662 r.m.s., and assumed that it scales as σ/\sqrt{n} , when n spaxels are
663 averaged. The generated synthetic spectra were then processed
664 as for the Ganymede data, and the resulting DIFF spectra were
665 cross-correlated with the forward model to obtain a cross correla-
666 tion function $\text{CCF}_{\text{noise}}$ for a spectrum containing only noise.
667 We then measured the standard deviation of the $\text{CCF}_{\text{noise}}$ curve.
668 Eighty random-noise synthetic spectra were processed in this
669 way, to derive a representative standard deviation σ_{CCFnoise} from
670 the median of the values obtained for each shot. For processed
671 Ganymede spectra, S/N_{CCF} is obtained by dividing the CCF at
672 $\delta v = 0$ by σ_{CCFnoise} .

673 The cross-correlation technique was applied on data averaged
674 over latitude bins (Figs. 2, C.1, C.2). Spectra with a Pearson
675 correlation coefficient $C_p > 0.3$ all display a CCF with $S/N_{\text{CCF}} >$
676 5 , and a maximum shifted by less than 1 spectel element. From
677 those criteria, the CO₂ exosphere is detected with good confi-
678 dence both in the northern and southern hemispheres of the lead-
679 ing and trailing sides of Ganymede. On the other hand, the S/N
680 (and inferred CO₂-gas signal) is low near the equator for both
681 hemispheres, indicating a more tenuous CO₂ exosphere in these
682 regions. The decrease of the CO₂ signal observed at the most polar
683 latitudes could be related to PSF blurring since spaxels prob-
684 ing extreme polar latitudes are near the limb of Ganymede disk.
685 However, this decrease is still observed after deconvolution with
686 modeled NIRSspec PSFs (Fig. M.1).

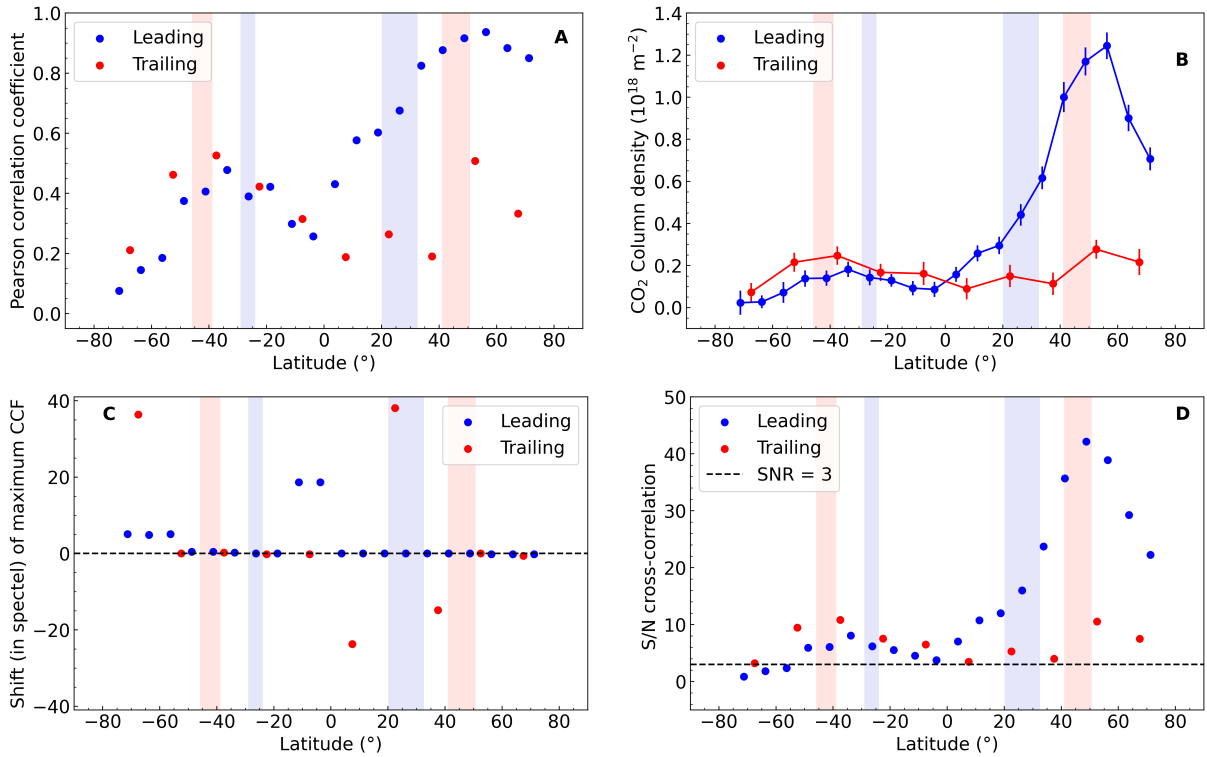


Fig. C.2. Study of 4.22–4.295 μm spectra averaged over latitude bins. A) Pearson correlation coefficient between residual CO₂ DIFF spectra and a synthetic DIFF spectrum which uses a CO₂ fluorescence synthetic spectrum at $T = 105$ K as input. B) CO₂ line-of-sight column density retrieved from the fit of CO₂ DIFF spectra. C) shift, in fraction of spectel, of the maximum of the cross-correlation function (CCF) between CO₂ DIFF spectra and the synthetic DIFF spectrum; secure detection is indicated when the shift is close to zero. D) S/N of the cross-correlation function at shift = 0. The S/N is obtained by computing the CCF_{noise} obtained by using as input a simulated noisy spectrum, with the r.m.s deduced from the ERR entry in the Level 3 data cube, and scaled in \sqrt{n} , where n is the number of averaged spaxels ($S/N = CCF/CCF_{noise}$ at shift = 0). In all plots, blue and red symbols correspond to the leading and trailing sides, respectively. The blue (resp. pink) vertical domains show the latitude range of the open-closed field-line boundaries for the leading and trailing sides, respectively, restricted to longitudes of 10–130° W (leading) and 210–330° W (trailing).

687 Appendix D: SMART-EVE excitation-radiative 688 transfer model

689 A non-LTE Stochastic Modeling of Atmospheric Radiative
690 Transfer-Exospheric Vibrational Excitation (SMART-EVE)
691 has been developed to calculate the ro-vibrational populations of the
692 (1) H₂O ν_2 mode (010) at 6.25 μm, and (2) CO₂ ν_3 mode (001)
693 at 4.25 μm. SMART-EVE solves the locally defined statistical
694 equilibrium equations (SEEs) for all the energy levels consid-
695 ered and the radiative transfer equations (RTEs) for all the bands
696 connecting these levels. Due to nonlinearities arising from radi-
697 ative transfer and/or collisional coupling, the resulting equa-
698 tion system is solved iteratively using the Accelerated Lambda
699 iteration approach which alternates SEE calculations involving
700 all the energy levels with RTE calculations involving all atmo-
701 spheric layers.

702 The 1D model of the atmosphere is described by the kinetic
703 gas temperature, assumed vertically uniform, and the gas density
704 which follows hydrostatic equation. The model assumes that the
705 atmosphere is illuminated by the Sun from the top, and by the
706 surface thermal emission and the reflected solar and atmospheric
707 radiance from below. The model parameters are: the column den-
708 sity and kinetic temperature T_{kin} of the atmosphere, the surface
709 temperature T_s and reflectance factor Ref , and the heliocentric
710 distance. Electron-impact excitation of CO₂ is not considered, as
711 most likely insignificant (Supplementary Information).

The radiative processes considered are spontaneous and
stimulated emissions, absorption of the upward thermal flux,
incident solar, and reflected solar and atmospheric irradiance
from the surface, as well as exchanges between layers. A single
collisional process is considered for the vibrational state, its
vibration-to-translation (V-T) relaxation/excitation in inter-
molecular collisions. However, vibrational de-excitation by
collisions is insignificant in Ganymede's exosphere (see Ap-
pendix G). It is assumed that rotational levels are at LTE at all
altitudes with a rotational temperature $T_{rot} = T_{kin}$.

The model is run from the surface up to 100 km, with 1-
km thick layers. The spectral data are taken from the HITRAN
database (Gordon et al. 2022). We considered only (010)–(000)
(H₂O) and (001)–(000) (CO₂) vibrational transitions, with a total
number of lines of 1017 for H₂O and 129 for CO₂. The solar
spectrum was taken from Paper I.

728 Appendix E: Determination of CO₂ column density

729 CO₂ line-of-sight column densities were derived using a two-
730 step approach. First, column densities were derived under the as-
731 sumption of fluorescence equilibrium and optically thin lines. In
732 the second step, a correction factor was applied, using prescrip-
733 tions obtained from the SMART-EVE model described above.

734 For CPU-time considerations, we used the Planetary Spec-
735 trum Generator (PSG) (Villanueva et al. 2018) for the first step.
736 Optically thin CO₂ ν_3 band fluorescence spectra at high spec-

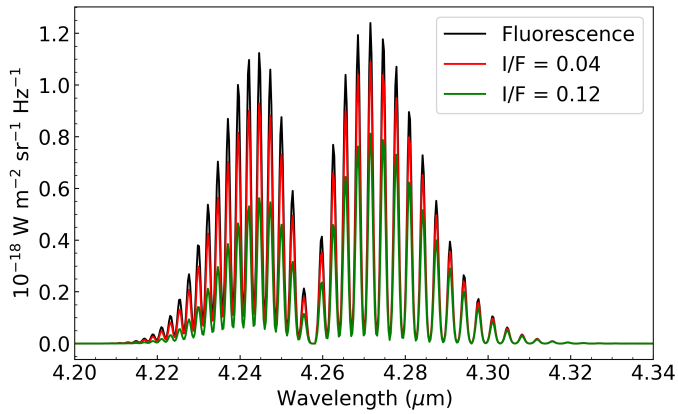


Fig. D.1. CO₂ simulated nadir spectra. Input model parameters are: CO₂ column density $N(\text{CO}_2) = 10^{18} \text{ m}^{-2}$, surface temperature $T_s = 145 \text{ K}$, gas rotational temperature $T_{\text{rot}} = 105 \text{ K}$, for I/F values of 0.04 (red) and 0.12 (green). The fluorescence spectrum (black) corresponds to $I/F = 0$ and $T_s = 0 \text{ K}$. Ganymede’s exosphere is described by hydrostatic equilibrium.

737 tral resolution (0.1 cm^{-1}) were generated (outputs for cometary
738 atmospheres) and downloaded for a range of rotational temper-
739 atures in steps of 1 K (and fixed column density). As done for
740 the forward model described above, they were combined with
741 Ganymede’s solid-state CO₂ band and synthetic DIFF spectra
742 were computed. This bank of synthetic spectra was utilized to
743 fit the Ganymede DIFF spectra using the Levenberg-Marquardt
744 algorithm (we used the *limfit* Python package), with a normal-
745 izing factor as free parameter. The rotational temperature was
746 set as a free parameter for the analysis of the high S/N spectra
747 of the north hemisphere of the leading side (Fig. H.1), and fixed
748 to 105 K elsewhere (i.e., equal to the inferred value in leading
749 north hemisphere, Appendix H). The CO₂ column density was
750 derived from the inferred normalizing factor. For the uncertainty
751 in the CO₂ column density, we used that provided by the *limfit*
752 package and derived from the covariance matrix.

753 Model simulations for the CO₂ ν_3 band (Fig. D.1) show that
754 spectral profiles from Ganymede’s exosphere are expected to be
755 less intense than in the assumption of cometary-like fluorescence
756 emission (case $Ref = 0$, $T_s = 0$), which neglects absorption of
757 surface reflected solar radiation by CO₂ gas, reflection of CO₂
758 gas emission on the surface, and surface thermal radiation. While
759 this latter process is not significant at $4.25 \mu\text{m}$, the other two pro-
760 cesses affect the total band intensity of the ν_3 band BA according
761 to:

$$762 \quad BA = BA_0 \times (1 - 4.2 \times I/F), \quad \text{for } N(\text{CO}_2) = 10^{17} \text{ m}^{-2} \quad (\text{E.1})$$

$$763 \quad BA = BA_1 \times (1 - 3.6 \times I/F), \quad \text{for } N(\text{CO}_2) = 10^{18} \text{ m}^{-2} \quad (\text{E.2})$$

$$764 \quad BA = BA_2 \times (1 - 2.1 \times I/F), \quad \text{for } N(\text{CO}_2) = 10^{19} \text{ m}^{-2} \quad (\text{E.3})$$

764 where I/F is the radiance factor on the surface, and BA_0 , BA_1 ,
765 BA_2 are equal to 4.10×10^{-8} , 4.27×10^{-7} , and $3.84 \times 10^{-6} \text{ W m}^{-2}$
766 sr^{-1} , respectively. BA_0 is consistent with the value of 4.06×10^{-8}
767 $\text{W m}^{-2} \text{sr}^{-1}$ retrieved from PSG (Villanueva et al. 2018) for opti-
768 cally thin cometary-like fluorescence emission at 4.95 au from
769 the Sun with $N(\text{CO}_2) = 10^{17} \text{ m}^{-2}$. Eqs E.1–E.3 were obtained
770 from multiple simulations fixing $T_s = 145 \text{ K}$ and $T_{\text{rot}} = 105 \text{ K}$,
771 and varying I/F .

772 We applied a correction factor intermediate between Eqs E.1
773 and E.2 (i.e., slope of -4.0 for the dependence with I/F) on
774 the CO₂ column density inferred assuming fluorescence equilib-
775 rium, using radiance factors I/F at $\sim 4.25 \mu\text{m}$ measured from
776 JWST (Paper I).

777 Appendix F: Electron impact excitation of CO₂

778 We made estimations for electron-impact excitation of the CO₂
779 ν_3 band using cross-sections from Itikawa (2002). Electron
780 populations were assumed to follow a Maxwellian distribution
781 around a mean temperature. For the total electron density and the
782 temperature, values that explain the highest UV brightnesses (OI
783 1356 Å) of 1000 R (Waite et al. 2024) measured for Ganymede
784 were used. Specifically, we assumed an electron temperature of
785 20 eV and a high number density of 2500 cm^{-3} . CO₂ emission
786 from this process is found to be more than two orders of magni-
787 tude lower than fluorescence emission. The CO₂ ν_3 band could
788 be excited by much cooler electrons, well below 10 eV. However,
789 information on these cold electrons is missing. Cross-sections
790 for electron-impact excitation of the CO₂ ν_3 band increase with
791 decreasing electron energy (Itikawa 2002). Using an electron
792 temperature of 1 eV and the same number density, CO₂ emis-
793 sion from electron impact excitation is only two times higher
794 than for 20 eV electrons.

795 Appendix G: CO₂ ν_3 -band collisional relaxation

796 We have evaluated the role of de-excitation of the CO₂ ν_3 band
797 by collisions with H₂O, O₂, and CO₂ versus spontaneous emis-
798 sion. The result is that these processes are not significant in
799 Ganymede’s exosphere. The rate for collisional de-excitation of
800 the CO₂ ν_3 band via CO₂-H₂O collisions is $1.2 \times 10^{-13} \text{ cm}^3/\text{s}$ at
801 120 K (Blauer & Nickerson 1973). The H₂O number density is
802 at most $1.4 \times 10^{10} \text{ cm}^{-3}$ at the surface, derived from hydrostatic
803 equilibrium for a water column density of $5 \times 10^{20} \text{ m}^{-2}$ (Roth
804 et al. 2021). This gives a collision rate of at most $1.7 \times 10^{-3} \text{ s}^{-1}$,
805 which is much lower than the spontaneous emission rate of the
806 ro-vibrational levels (on the order of 400 s^{-1}). So the quenching
807 is negligible.

808 The rates for de-excitation of CO₂ ν_3 band via collisions with
809 O₂ and CO₂ are much lower than for CO₂-H₂O collisions. So
810 these collisional processes are still less significant.

811 Appendix H: Rotational temperature of CO₂

812 For fluorescence emission, the relative intensities of the ro-
813 vibrational lines of the CO₂ ν_3 band are set by the population
814 distribution in the ground vibrational state, described by a Boltz-
815 mann distribution at the rotational temperature T_{rot} . Rotational
816 temperatures of CO₂ derived on the northern latitudes ($>30^\circ \text{ N}$)
817 of the leading hemisphere are shown in Fig. H.1 and are on the
818 order of 105–110 K (see Appendix B for details on how T_{rot} was
819 derived). This is slightly lower than the surface temperature of
820 Ganymede at these latitudes (from 120 to 140 K, Fig. K.1). This
821 rotational temperature possibly reflects the kinetic temperature
822 of the exosphere at low altitudes where collisions with the major
823 gas (H₂O or CO₂) are still efficient enough to thermalize CO₂
824 molecules. Alternatively, it might reflect the rotational energy of
825 the CO₂ molecules when they left the surface, and be representa-
826 tive of the temperature of the surface where CO₂ molecules were
827 released. The CO₂ molecule has no dipole moment, so radiative
828 rotational decay within the ground vibrational state does not take

829 place. The rotation temperature is expected to increase with resi-
 830 dence time in the atmosphere due to radiative decay from the ex-
 831 cited vibrational states. However, one should mention that during
 832 their residence time in the exosphere (at most 18 h, which is the
 833 CO₂ lifetime set by electron-impact ionization), CO₂ molecules
 834 undergo at most 7 fluorescence cycles. Based on fluorescence
 835 calculations for cometary atmospheres, CO₂ molecules reach a
 836 warm fluorescence equilibrium only after about 3500 fluores-
 837 cence cycles at 5 au from the Sun Crovisier (1987). In summary,
 838 the measured T_{rot} should reflect the thermal environment where
 839 last thermalizing collisions occurred, or the excitation state of
 840 the molecules when they left the surface.

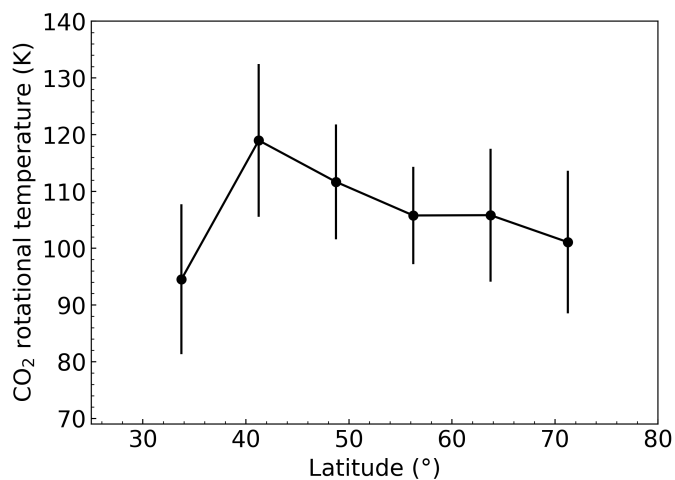


Fig. H.1. CO₂ rotation temperature in the north hemisphere of the leading hemisphere. Spaxels within latitude bins of width 7.5° were averaged. Values were derived from the fitting of DIFF spectra using as model fluorescence emission with T_{rot} as a free parameter (Appendix B). The weighted mean value is $T_{\text{rot}} = 107 \pm 5$ K.

841 Appendix I: H₂O analysis

842 We analysed MIRI/MRS Channel-1 spectra obtained by either 1)
 843 averaging spaxels around the subsolar point, namely eight spax-
 844 els for which the solar zenith angle (SZA) is less than 15° at
 845 the center of the spaxel; 2) averaging seven spaxels covering the
 846 region of the leading hemisphere where the CO₂ exosphere is
 847 prominent. Neither one shows any hint of the presence of water
 848 lines (Fig. I.1) and the nondetection of H₂O was further con-
 849 firmed by applying the cross-correlating technique using a for-
 850 ward model of a synthetic spectrum of H₂O computed with the
 851 SMART-EVE code.

852 In the exosphere of Ganymede, the thermal radiation from
 853 the surface competes with the Sun's direct radiation for the ex-
 854 citation of the H₂O ν_2 band at 6.2 μm (Paper I). In addition,
 855 in nadir viewing, absorption of the radiation from Ganymede's sur-
 856 face by the H₂O exosphere might compete with ν_2 fluorescence
 857 emission, so that the band might be in absorption under certain
 858 conditions and a simple fluorescence model would not apply.
 859 Therefore, we used the SMART-EVE model described above to
 860 derive upper limits on the H₂O column density ($N(\text{H}_2\text{O})$).

861 Radiance factor values of 0.04 and 0.08 were assumed for the
 862 leading and trailing hemispheres, respectively (see Fig. 26 of Pa-
 863 per I). The surface temperature was chosen such that the bright-
 864 ness temperature in the synthetic spectra matches the T_{BB} value
 865 at 6.2 μm measured on the MIRI spectrum. For the "subsolar"
 866 spectra (SZA < 15°), T_s (and T_{BB}) are closed to 155 K (leading

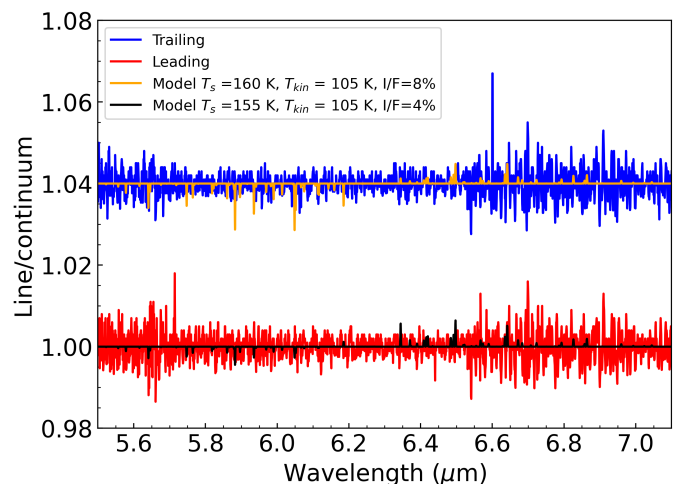


Fig. I.1. Continuum-divided spectra of Ganymede observed with MIRI and synthetic H₂O spectra. Spectra for the leading and trailing sides are shown in red and blue, respectively, with the spectrum of the trailing side shifted vertically. Spaxels for which the solar zenith angle is less than 15° at the center of the spaxel have been averaged. Synthetic spectra are superimposed, with input parameters indicated in the legend (Appendix I) and $N(\text{H}_2\text{O}) = 10^{20} \text{ m}^{-2}$. The Ganymede spectra do not show any hint of H₂O lines.

867 and 160 K (trailing). For the spectrum extracted at the position
 868 of the CO₂ northern source, T_s is about 140 K. Synthetic spectra
 869 for the subsolar region are shown in Fig. I.1. Ro-vibrational lines
 870 at $\lambda < 6.2 \mu\text{m}$ are expected in absorption whereas emission lines
 871 are expected at $\lambda > 6.2 \mu\text{m}$. As a matter of fact, the vibrational
 872 temperature of the ν_2 band (mainly controlled by solar IR pump-
 873 ing) is ~ 158 – 159 K, i.e. very close to the brightness temperature
 874 near 6.4 μm . The change from absorption to emission regimes is
 875 related to the fact that the vibrational temperature is close to the
 876 wavelength-dependent brightness temperatures near 6.2 μm .

877 Table I.1 presents measured 1- σ uncertainties for the H₂O
 878 band area in the 5.7–6.2 and 6.2–7.1 μm spectral ranges, consid-
 879 ering the 10–15 expected strongest lines (with intensities > 0.2
 880 the intensity of the strongest line). From the measured band areas
 881 in each wavelength window, we derived a 3 σ upper limit for
 882 line-of-sight $N(\text{H}_2\text{O})$, using SMART-EVE model with appropri-
 883 ate parameters. The results were then combined. The final results
 884 are given in Table I.1 for two values (105 and 130 K) of the H₂O
 885 rotational temperature.

886 Appendix J: Open-closed field-line boundary

887 The OCFB location is determined through magnetohydrody-
 888 namic modeling of Ganymede's magnetosphere similar to the
 889 method described in Duling et al. (2022). Due to the variation of
 890 the upstream magnetic field and plasma density at Ganymede's
 891 position relative to the Jovian current sheet, the OCFB loca-
 892 tion can oscillate with an amplitude ranging between 2 to 6 de-
 893 gree latitude during Jupiters's approximative 10-h rotation pe-
 894 riod (Saur et al. 2015). We modeled the OCFB analogous (Dul-
 895 ing et al. 2022) by adapting the upstream conditions to estimates
 896 for the times of the JWST observations. During the observation
 897 of the leading side, Ganymede was above the center of the cur-
 898 rent sheet and we used 61 amu/cm³ and (−11, −66, −79)nT for the
 899 upstream plasma mass density and magnetic field respectively.
 900 During the trailing side observation Ganymede was at the cen-

Table I.1. H₂O and CO₂ line-of-sight column densities in selected Ganymede's areas.

Region ^a	H ₂ O band area (1-σ) ^b	H ₂ O band area (1-σ) ^c	$N(\text{H}_2\text{O}) (3\sigma)^d$	$N(\text{H}_2\text{O}) (3\sigma)^d$	$N(\text{CO}_2)^f$
	$\lambda < 6.2 \mu\text{m}$ (W m ⁻² sr ⁻¹)	$\lambda > 6.2 \mu\text{m}$ (W m ⁻² sr ⁻¹)	$T_{\text{rot}} = 105 \text{ K}$ (m ⁻²)	$T_{\text{rot}} = 130 \text{ K}$ (m ⁻²)	$T_{\text{rot}} = 105 \text{ K}$ (m ⁻²)
Leading CO ₂ source	$< 3.1 \cdot 10^{-8}$	$< 1.0 \cdot 10^{-7}$	$< 2.0 \cdot 10^{19}$	–	$1.0 \cdot 10^{18}$
Leading SZA < 15°	$< 4.7 \cdot 10^{-8}$	$< 2.2 \cdot 10^{-7}$	$< 6.8 \cdot 10^{19}$	$< 1.7 \cdot 10^{20}$	$< 1.9 \cdot 10^{17}$
Trailing SZA < 15°	$< 6.8 \cdot 10^{-8}$	$< 3.4 \cdot 10^{-7}$	$< 3.1 \cdot 10^{19}$	$< 4.6 \cdot 10^{19}$	$< 2.5 \cdot 10^{17}$

^a Using extracted spectra from either the subsolar region (Solar Zenith Angle SZA < 15°, average of 8 pixels for MIRI, 27 pixels for NIRSpec) or from the region with large CO₂ gas emission (leading, 40–65°N, 46–100°W, 7 pixels for MIRI, 15 pixels for NIRSpec). ^b Using the most intense 10–15 ro-vibrational lines expected in absorption in the 5.7–6.2 μm spectral range. ^c Using the most intense 10–15 ro-vibrational lines expected in emission in the 6.2–7.1 μm spectral range. ^d 3σ upper limits on H₂O line-of-sight column density combining upper limits obtained for the two spectral ranges (< 6.2 μm and > 6.2 μm). ^f Upper limits are 3σ.

901 ter of the current sheet and we used 100 amu/cm³ and (–18, –6,
902 –79)nT.

903 Appendix K: CO₂, H₂O Ganymede exospheric 904 model

905 We simulated the CO₂ exosphere using the Exospheric Global
906 Model (EGM), a multi-species Monte Carlo model describing
907 the fate of test particles in a gravitational field, interacting with
908 a surface or an atmosphere and subject to sources of ioniza-
909 tion and dissociation. EGM has been extensively used to model
910 the exospheres of H₂O and related species (e.g., O₂, H) in vari-
911 ous objects, in particular Ganymede (Leblanc et al. 2017, 2023).
912 We considered two possible mechanisms of ejection of the CO₂
913 molecules from the surface: i) sputtering, i.e. ejection following
914 bombardment of H₂O ice containing CO₂ molecules by the in-
915 cident Jovian energetic ions and electrons; and ii) sublimation
916 of the CO₂ molecules from Ganymede surface. We considered
917 the release of CO₂ either from the sublimation of pure CO₂ ice
918 or from the sublimation of H₂O ice containing CO₂ molecules.
919 We took into account that CO₂ molecules re-impacting cold ar-
920 eas of the surface eventually recondense. The H₂O exosphere is
921 also computed. The calculated images from the simulations (e.g.,
922 Fig. 3) consider the orbital position of Ganymede around Jupiter
923 at the time of the JWST observations and the viewing geometry
924 of JWST observations (for the observations of the leading hemi-
925 sphere, sub-observer coordinates were 2°N, 72°W). Convolution
926 with a FWHM = 0.185'' PSF is applied (Appendix M). Line-of-
927 sight CO₂ column densities averaged over latitude bins of 7.5°
928 or 15° were computed for comparison with the data shown in
929 Fig. 2. For the study of the CO₂ exosphere above the north po-
930 lar cap of the leading hemisphere, we extracted the longitudinal
931 variation of the CO₂ column density for latitudes in the range
932 42–62° N.

933 **Sublimation:** For a CO₂ release associated with the subli-
934 mation of water ice, the release rate is in proportion with the
935 H₂O sublimation rate (cm⁻² s⁻¹):

$$936 F(\text{CO}_2) = f_c \times q_{\text{CO}_2} \times 2.17 \cdot 10^{32} \frac{e^{-\frac{U_0}{k_B T_s}}}{\sqrt{T_s}} \quad (\text{K.1})$$

$$937 F(\text{H}_2\text{O}) = q_{\text{H}_2\text{O}} \times 2.17 \cdot 10^{32} \frac{e^{-\frac{U_0}{k_B T_s}}}{\sqrt{T_s}}, \quad (\text{K.2})$$

936 where $U_0/k_B = 5950 \text{ K}$, and $q_{\text{H}_2\text{O}}$ is the areal surface fraction of
937 H₂O. The relative abundance of CO₂ in the sublimated gases
938 (in number) is $q_{\text{CO}_2}/q_{\text{H}_2\text{O}}$. The description of $F(\text{H}_2\text{O})$ follows

Leblanc et al. (2023). T_s is the surface temperature. f_c is a factor
939 introduced to reproduce the CO₂ JWST data.

940 For the sublimation of CO₂ ice, the sublimation rate (cm⁻² s⁻¹)
941 is given by:
942

$$943 F(\text{CO}_2) = f_c \times \frac{N_{\text{tot}} q_{\text{CO}_2}}{\tau_0 \sqrt{T_s}} e^{-\frac{U_1}{k_B T_s}}, \quad (\text{K.3})$$

944 where $N_{\text{tot}} = 10^{18} \text{ cm}^{-2} \text{ s K}^{0.5}$ is determined from a fit of the
945 polynomial relation of CO₂-ice vapor pressure with tempera-
946 ture (Fray & Schmitt 2009) and using $U_1/k_B = 2860 \text{ K}$ (surface
947 binding energy for CO₂ on H₂O ice, (Sandford & Allamandola
948 1990)) and $\tau_0 = 3.45 \cdot 10^{-13} \text{ s}$ (Sandford & Allamandola 1990).
949 f_c is a factor introduced to reproduce the JWST data.

950 **Sputtering:** The ejection of CO₂ molecules by sputtering is
951 described by the efficiency by which CO₂ molecules are emitted
952 from a surface when an incident ion or electron impacts the sur-
953 face with a given energy. We hypothesized that CO₂ molecules
954 are trapped in/on H₂O ice, so we assumed that the sputtering
955 yield follows the same temperature dependence as for H₂O, and
956 used the same definition as for H₂O (Cassidy et al. 2013; Leblanc
957 et al. 2023):

$$958 Y(\text{CO}_2) = f_c \times Y_0 \times (1 + Y_{00} \times e^{-\frac{U_{00}}{k_B T_s}}), \quad (\text{K.4})$$

959 with $Y_0 = 1200$. We made the assumption that CO₂ molecules
960 are released into the exosphere along with H₂, O₂, H₂O₂ and
961 H₂O molecules ejected when pure H₂O ice is bombarded, there-
962 fore U_{00} and Y_{00} are set to be the same as for the bombard-
963 ment of pure H₂O ice (Famá et al. 2008): $U_{00} = 0.06 \text{ eV}$ (700
964 K), $Y_{00} = 220$. As for the energy and angular distributions of
965 the CO₂ molecules when ejected from the surface, we followed
966 the approach used for sputtered O₂ in Leblanc et al. (2017) and
967 assumed a Maxwell–Boltzmann energy distribution at the local
968 surface temperature. Regarding the intensity and spatial distribu-
969 tion of the Jovian ions impacting the surface, we assumed a given
970 ion flux of 10⁶ particles/cm²/s derived from Cassidy et al. (2013)
971 as in Leblanc et al. (2017), impacting Ganymede's surface only
972 in the open-field-line regions. Electron impacts are not consid-
973 ered. The flux of the CO₂ molecules released at a given posi-
974 tion on Ganymede's surface is therefore the product of $Y(\text{CO}_2)$
975 (Eq. K.4) times q_{CO_2} times the flux of impacting particles. The
976 flux of H₂O follows the same equation, using $q_{\text{H}_2\text{O}}$ instead. A
977 multiplying factor f_c is introduced in Eq. K.4 with respect to
978 Cassidy et al. (2013) and Leblanc et al. (2023) that is adjusted
979 to reproduce the CO₂ column density measured by JWST. This
980 factor is also applied to the flux of H₂O sputtered molecules. In
981 our model, sputtering of water ice is assumed to release mainly
982 H₂O molecules with a ratio H₂O/O₂ = 20 (Leblanc et al. 2017;
983 Cassidy et al. 2013).

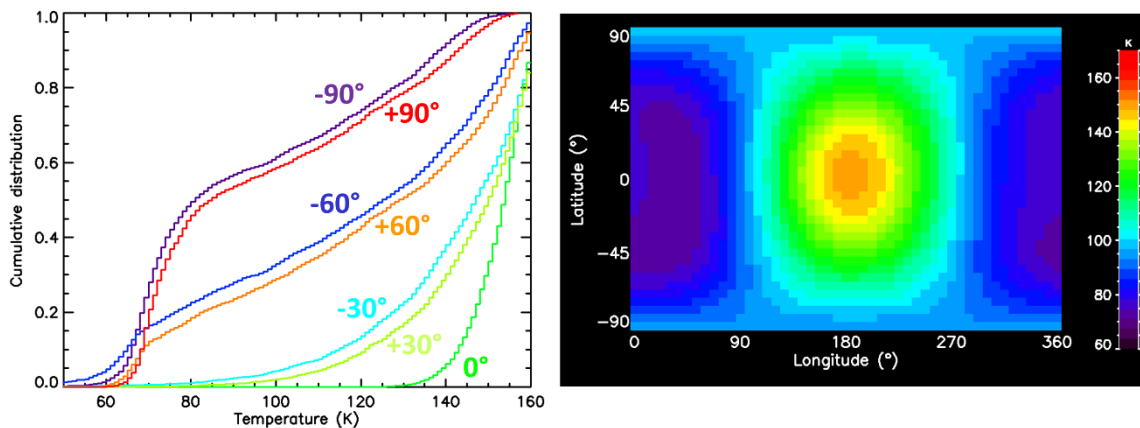


Fig. K.1. Ganymede's surface temperature used in EGM model, representative of the leading hemisphere. Left panel: facet temperature distribution (cumulative probability) of the surface temperatures at 12 h local time for various latitudes indicated in the plot. Right panel: latitude/longitude map of the average surface temperature with the subsolar point being at a latitude of 2°N (as for JWST observations, Paper I) and longitude of 180°.

982 **Surface adsorption:** To determine the fate of a CO₂ molecule re-impacting the surface, we define the CO₂ residence time at the surface as:

$$\tau = \tau_0 e^{\frac{U_1}{k_B T_s}} \quad (\text{K.5})$$

985 where $U_1/k_B = 2860$ K is the binding energy for CO₂ adsorbed on H₂O ice, and $\tau_0 = 3.45 \cdot 10^{-13}$ s (Sandford & Allamandola 1990). We considered that when the CO₂ residence time is longer than the model time step (0.25 s), any particle hitting the surface gets trapped in the surface. We then calculated at each step and for each trapped particle a probability to be re-ejected as being equal to the ratio between the time step of the simulation and the residence time calculated from the surface temperature at the position of the particle. This probability is then compared to a random number between 0 and 1 and if higher than this random number, the particle is re-emitted into the exosphere. We checked that the results are not sensitive to the model time step.

997 **Surface temperature:** In Leblanc et al. (2017) and Leblanc et al. (2023), the Ganymede's surface temperature was calculated using a 1-D heat conduction model. Such description had some limitations, in particular it ignored surface roughness that leads to a distribution of facet temperatures (instead of a single temperature) at a given latitude, longitude and local time. Bockelée-Morvan et al. (2024) (Paper I) showed that matching the JWST/MIRI brightness temperature maps, in particular the low to high latitude and the noon to dawn or dusk temperature contrasts, requires considering surface roughness effects. In the framework of a model for the distribution of slopes inherited from Hapke (1984), they found that the data could be fit by invoking mean slope angles $s = 15^\circ - 20^\circ$ on the trailing side and $20^\circ - 25^\circ$ on the leading side, with some variations depending on the adopted surface albedo model. Here we adopted the following parameters, relevant to the leading side: $s = 25^\circ$, Bond albedo = 0.30, thermophysical parameter $\Theta = 0.3$ (i.e. thermal inertia $\Gamma = 22.5$ SI units). We used a spatially constant Bond albedo to keep the number of free parameters tractable. Such rough temperature distributions were calculated on a 37×48 latitude \times local time (or longitude) grid, i.e. with a 5° latitude and 0.5 h local time step. Figure K.1 (left) shows examples of cumulative facet temperature distributions at noon local time and various latitudes, while the right panel shows the facet-averaged temperature map, where the maximum temperature is at 12.5 h local

time. The multiplicity of temperatures at a given latitude/local time enables condensation in regions where it would not be expected without surface roughness. At the equator, the probability to find a surface element at a temperature smaller than 73 K (the theoretical condensation temperature of CO₂ at Ganymede atmospheric pressure of 1 pbar) is zero, even in presence of surface roughness. However, the probability of encountering temperatures lower than 73 K increases with latitude, to 1% at +30°, 12% at +60° and 30% at +90°.

For describing the temperature of the surface of the trailing side (used for the calculations shown in Appendix L.4), we adopted the following parameters, which fit at best the JWST/MIRI brightness temperature map of this hemisphere: $s = 20^\circ$, Bond albedo = 0.20, thermophysical parameter $\Theta = 0.3$.

We stress that, as indicated in Paper 1, our thermal model describes roughness purely as a slope effect, and does not account for other more complex effects associated with topography, such as shadowing and self-heating due to scattering and re-absorption of solar and thermal radiation within craters, as done for investigating cold traps for water ice on the Moon (Hayne et al. 2021; Davidsson & Hosseini 2021). Applying such more advanced thermophysical models is left to future investigations.

Appendix L: Simulated exospheres from EGM simulations

L.1. CO₂ gas spreading

A question to address is the localized character of Ganymede's CO₂ exosphere. Indeed, CO₂ does not condense efficiently at the typical Ganymede's surface temperatures, even in the polar regions (100-110 K), and therefore could spread out over the whole illuminated disk, possibly condensing only in the non-illuminated areas. To study the spreading of CO₂ molecules, we performed EGM simulations (Appendix K) assuming that CO₂ is released by the sublimation of CO₂ ice from a small surface area (300×300 km) at 52°N. The calculations were performed using a distribution of facet temperatures for each location, as computed with our thermal model with surface roughness (Appendix K), and, for comparison, using instead the facet-average temperature map (Fig. K.1, right). Figure L.1 shows the vertical CO₂ column density in the two cases. It shows that the resulting

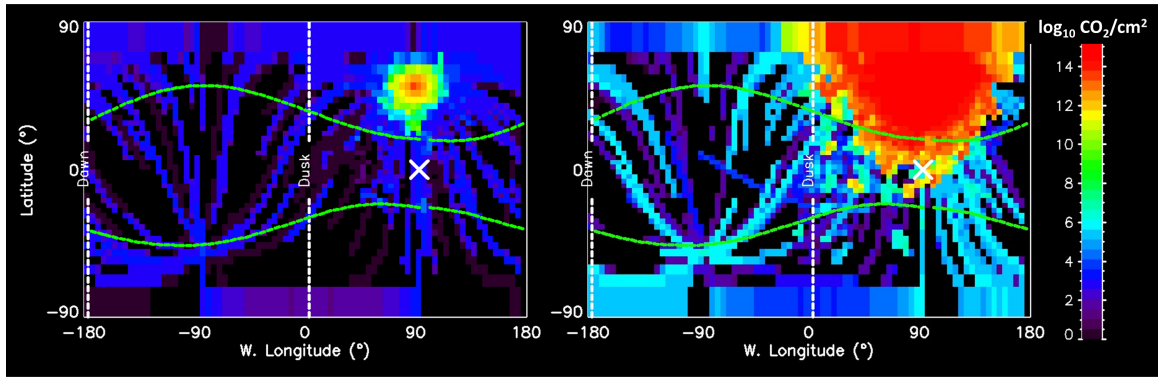


Fig. L.1. Vertical CO₂ column density using a distribution of temperature at each location (rough surface, left panel) or the mean temperature (right panel). The simulations consider the sublimation of CO₂ ice from a 300×300 km region at 52°N, with $q_{\text{CO}_2} \times f_c = 3 \times 10^{-14}$.

1061 atmospheric distribution is quite different for the rough surface.
 1062 The migration distance is much smaller in this case, showing
 1063 that the diffusion of CO₂ molecules is substantially controlled
 1064 by the ability to condense on cold traps. These cold traps are
 1065 probably the discrete patches of optically thick ice, preferentially
 1066 located on pole-facing slopes, that constitute the polar cap (Khu-
 1067 rana et al. 2007). The limited horizontal spreading of CO₂ gas
 1068 indicates that local column-density maxima are associated with
 1069 local sources.

1070 L.2. CO₂ exosphere: Leading CO₂ source only

1071 The most significant feature of Ganymede's CO₂ exosphere be-
 1072 ing the large excess in the northern hemisphere of leading side,
 1073 our simulations (see Appendix K for model description) were
 1074 designed to reproduce this feature. Specifically, we calculated
 1075 line-of-sight column density maps $N(\text{CO}_2)$, and extracted latitu-
 1076 dinal and longitudinal profiles of $N(\text{CO}_2)$ for comparison with
 1077 observations. Model simulations were performed assuming q_{CO_2}
 1078 = 1% in a northern cap extending from lat_c to 90° in latitude and
 1079 ranging from 0 to 180°W in longitude. Elsewhere, q_{CO_2} was set
 1080 to 0. The input value $q_{\text{CO}_2} = 1\%$ was set as it is consistent within
 1081 a factor of a few with the rough estimation of the CO₂ abundance
 1082 at the surface based on the depth of the CO₂-solid 4.3 μm band
 1083 (CO₂/H₂O ~ 1% in mass, Paper I). The limiting latitude lat_c and
 1084 the correction factor f_c to the CO₂ flux were adjusted to best re-
 1085 produce the position in latitude and value of the column-density
 1086 peak in the latitudinal profile of $N(\text{CO}_2)$ shown in Fig. 2.

1087 Column density maps obtained for sputtering, CO₂ release
 1088 associated with H₂O sublimation and sublimation of CO₂ ice
 1089 (Appendix K) are shown in Fig. L.2 (and in the main text Fig. 3
 1090 for the first two production mechanisms). EGM latitudinal pro-
 1091 files of line-of-sight column densities are compared to observa-
 1092 tions in the left panels of Fig. L.2. Longitudinal variations for
 1093 latitudes in the range 42–62° N (i.e., encompassing the northern
 1094 region of the leading hemisphere with CO₂ gas enhancement)
 1095 are compared in the right-hand panels of Fig. L.2. Table L.1
 1096 lists model input parameters, and average column densities in
 1097 the subsolar region and so-called "Leading CO₂ source" defined
 1098 in Table I.1. For CO₂ release associated with H₂O sublimation
 1099 (top panels), the latitudinal profile is reproduced for $lat_c = 50^\circ\text{N}$
 1100 and multiplying the flux of CO₂ molecules by $f_c = 260$ (as $f_c \times$
 1101 $q_{\text{CO}_2} = 260 \times 0.01 = 2.6$, this corresponds to a CO₂/H₂O relative
 1102 abundance of 5 for an H₂O areal ice fraction of 50%). Since the
 1103 H₂O sublimation flux is highly dependent of the surface temper-
 1104 ature (Eq. K.2) and is therefore strongly favored at low latitudes,

1105 lat_c must be close to the latitude at which the peak of the CO₂
 1106 column density is observed (Fig. 1). For the CO₂-ice sublima-
 1107 tion case (middle panels), lat_c is also close to 50°N, and $f_c = 3$
 1108 $\times 10^{-12}$. For the sputtering scenario (bottom panels), a limiting
 1109 latitude $lat_c = 40^\circ\text{N}$ best reproduces the latitudinal trend of the
 1110 column density (a too narrow distribution in latitude is obtained
 1111 for $lat_c = 50^\circ\text{N}$), and the flux of the sputtered CO₂ molecules
 1112 had to be multiplied by $f_c = 382$.

As shown in Fig. L.2, the sputtering only scenario (panels e
 1113 and f) provides a better fit of the spatial distribution of CO₂ exo-
 1114 sphere than sublimation. Especially, for the sublimation scenar-
 1115 ios, a strong variation with longitude (i.e., local time) is obtained
 1116 whereas the diurnal variation is flatter and almost consistent with
 1117 the observations for sputtering. This is essentially due to the
 1118 difference in the temperature dependence of these mechanisms
 1119 (Eqs K.1, K.3, K.4). However, the peak of the CO₂ line-of-sight
 1120 column-density distribution for sputtering is more shifted toward
 1121 the afternoon (~13.4 h) than in the sublimation cases (~13.1 h)
 1122 and for the observed peak (~12 h).
 1123

L.3. H₂O exosphere

1124 EGM simulations of Ganymede's H₂O exosphere were already
 1125 performed by Leblanc et al. (2017, 2023), but the used surface
 1126 temperature model did not consider surface roughness, unlike
 1127 the present calculations. Figure L.3 displays the H₂O column
 1128 density as seen from JWST for the sublimation (left panel) and
 1129 sputtering (right panel) cases. The H₂O ice areal surface frac-
 1130 tion $q_{\text{H}_2\text{O}}$ is set to 20% all over the surface, a value which is
 1131 consistent with measured water ice abundances on the leading
 1132 side for latitudes $\leq 30\text{--}40^\circ$ Ligier et al. (2019). For latitudes of
 1133 40–50°N, values of 40–50% would be more appropriate Ligier
 1134 et al. (2019). As expected the sublimation of H₂O follows the
 1135 surface temperature distribution. A North/South asymmetry can
 1136 be clearly seen which is driven by the small asymmetry in sur-
 1137 face temperature associated with the positive subsolar latitude
 1138 (see Fig. K.1). A dawn to dusk asymmetry with higher H₂O col-
 1139 umn densities toward the dusk is also present. A similar dawn-
 1140 dusk asymmetry, related to surface thermal inertia, is present for
 1141 the CO₂ simulated exosphere (Fig. 3, left panel).
 1142

The calculated line-of-sight H₂O column densities in the
 1143 leading subsolar region (solar zenith angle SZA < 15°) and so
 1144 called "Leading CO₂ source" are given in Table L.1. They are
 1145 below the upper limits set by JWST (7–17×10¹⁹ m⁻² for subso-
 1146 lar, 2×10¹⁹ m⁻² for CO₂ source region, Table I.1), summing the
 1147 contributions from sputtering and sublimation. When consider-
 1148

Table L.1. Line-of-sight column densities from EGM simulations.

Models/Region	$q_{\text{CO}_2}^{(a)}$ (%)	$lat_c^{(a)}$ (°)	$f_c(\text{CO}_2)^{(b)}$	$N(\text{CO}_2)$ (m ⁻²)	$q_{\text{H}_2\text{O}}$ %	$f_c(\text{H}_2\text{O})$	$N(\text{H}_2\text{O})$ (m ⁻²)
<i>H₂O-ice sublimation, with CO₂ release</i>							
Leading North source	1	50	260	9.0×10^{17}	20	–	1.4×10^{18}
Leading SZA < 15°	1	50	260	$4.1 \times 10^{10*}$	20	–	4.1×10^{19}
<i>CO₂ ice sublimation</i>							
Leading North source	1	50	3×10^{-12}	8.8×10^{17}	–	–	–
Leading SZA < 15°	1	50	3×10^{-12}	$4.4 \times 10^{15*}$	–	–	–
<i>Sputtering only</i>							
Leading North source	1	40	382	9.9×10^{17}	20	382	8.2×10^{18}
Leading SZA < 15°	1	40	382	$2.6 \times 10^{15*}$	20	382	2.6×10^{17}

^(a) q_{CO_2} in a northern cap covering $lat_c - 90^\circ$ in latitude and ranging from 0 to 180°W in longitude. Elsewhere, q_{CO_2} is set to 0.

^(b) Correction factor to simulated CO₂ flux from the surface to reproduce the CO₂ line-of-sight column density peak in the latitude profile (Fig. 2).

^(*) Values are low because $q_{\text{CO}_2} = 0$ for latitudes < lat_c .

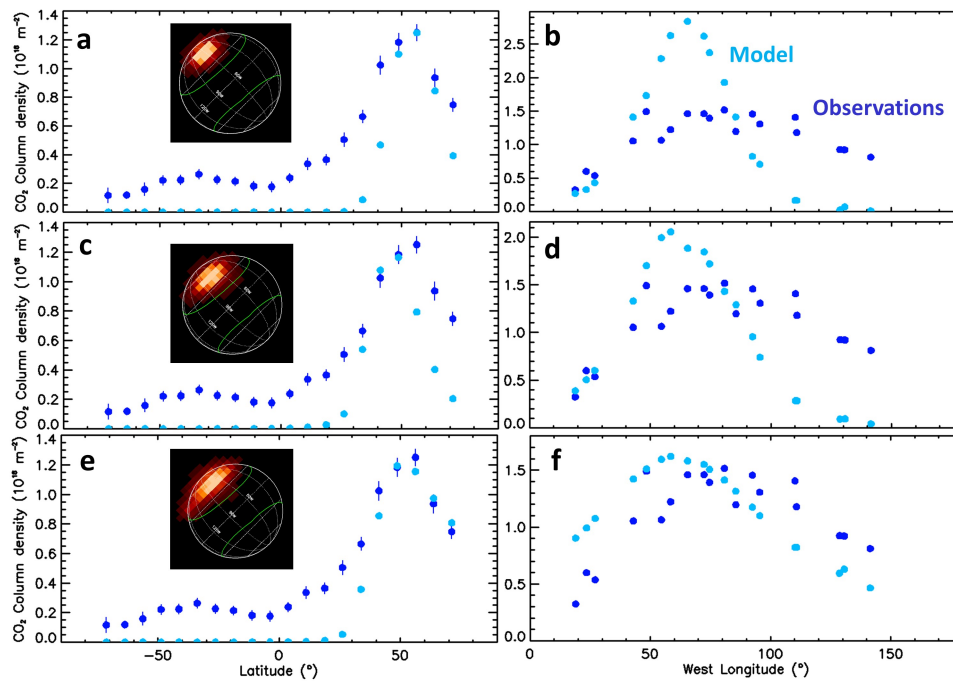


Fig. L.2. CO₂ gas line-of-sight column density as a function of latitude (left) and longitude (right) for the leading side. Light blue symbols show model results from EGM and dark blue symbols refer to JWST observations. Top panels (a, b): CO₂ release associated to H₂O sublimation with surface flux $f_c \times q_{\text{CO}_2} = 2.6$ at latitudes > 50°N and $q_{\text{CO}_2} = 0$ elsewhere. Middle panels (c, d): CO₂ release associated to CO₂ ice sublimation with surface flux $f_c \times q_{\text{CO}_2} = 3.0 \times 10^{-14}$ at latitudes > 50°N and $q_{\text{CO}_2} = 0$ elsewhere. Bottom panels (e, f): sputtering only with surface abundance $q_{\text{CO}_2} = 1\%$ at latitudes > 40°N, and $q_{\text{CO}_2} = 0$ elsewhere, and a multiplying factor to surface CO₂ flux $f_c = 382$. In the left panels (a, c, e) column densities are averages in latitude bins of 7.5°. Longitudinal variations shown in right panels (b, d, f) consider latitudes in the range 42–62°N (i.e., encompassing the northern region of the leading hemisphere with CO₂ gas enhancement). Calculated CO₂ column density maps for all three cases are shown in the left panels.

1149 ing a more appropriate value of $q_{\text{H}_2\text{O}} = 40\text{--}50\%$ for the northern
 1150 region of the leading hemisphere, the modeled column density
 1151 for this region is of the order of the JWST upper limit. The value
 1152 obtained for the subsolar region ($4.1 \times 10^{19} \text{ m}^{-2}$) is a factor of
 1153 7 above the minimum value derived from HST OI data for the
 1154 leading hemisphere ($6 \times 10^{18} \text{ m}^{-2}$, Roth et al. (2021)).

1155 We stress that calculated H₂O sputtered fluxes are under the
 1156 hypothesis that H₂O is the major species released by sputtering
 1157 of H₂O ice Cassidy et al. (2013). However, the major mass loss
 1158 from water ice by particle bombardment might not be H₂O, as

assumed here, but rather via the ejection of O₂ and H₂ (or at
 1159 least in significant proportion) according to laboratory experi-
 1160 ments Teolis et al. (2017). Hence, H₂O sputtered fluxes given in
 1161 Table L.1 can be considered as upper limits. This reinforces our
 1162 conclusion that JWST H₂O upper limits measured in the north
 1163 polar cap of the leading hemisphere are fully consistent with ex-
 1164 pectations. 1165

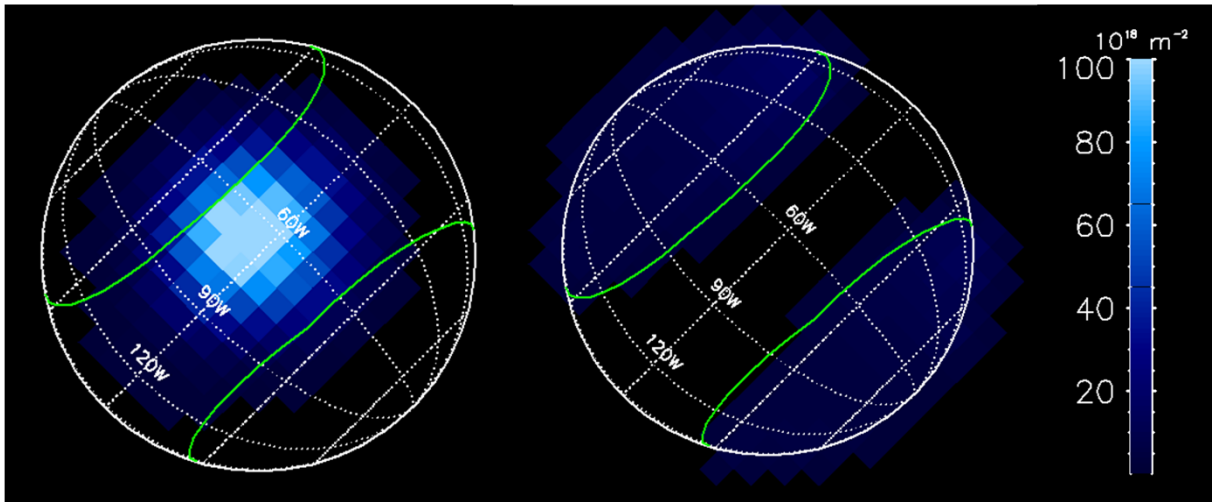


Fig. L.3. Calculated line-of-sight column-density maps of the H_2O exosphere of Ganymede (in 10^{18} m^{-2}). The green lines display the boundary between open and closed field lines (OCFBs). Left panel: sublimation only source. Right panel: sputtering only source with $f_c = 382$. The H_2O areal surface fraction is set to $q_{\text{H}_2\text{O}} = 20\%$. The subsolar point is at 2.6°N , 82°W .

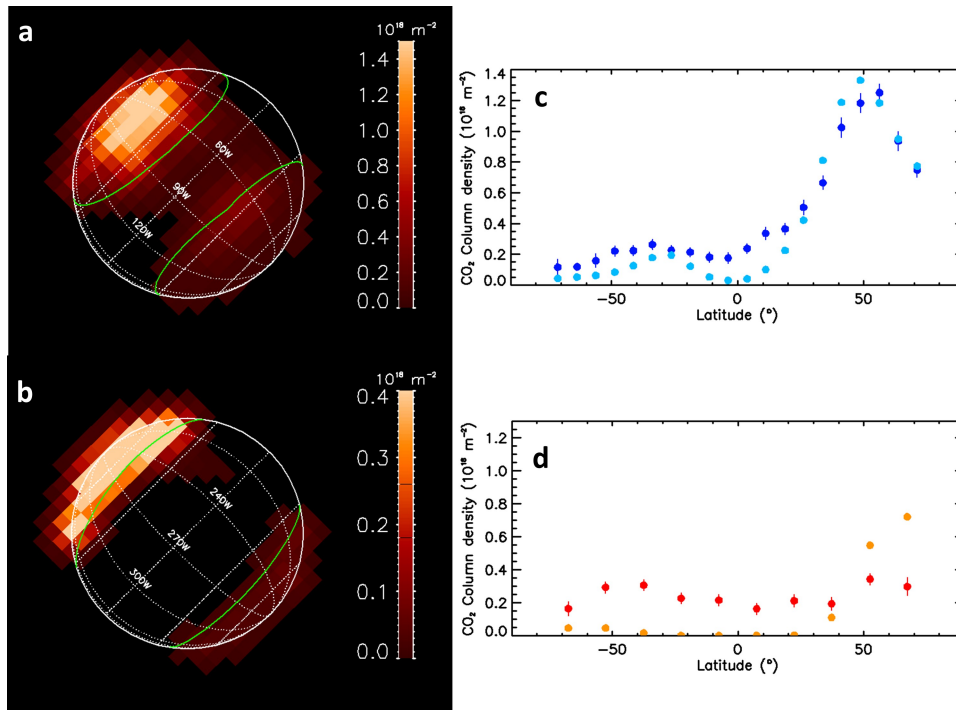


Fig. L.4. Simulation of the entire CO_2 exosphere formed by sputtering only. No sputtering is simulated inside the closed-field-line region. Input parameters are given in the text. Panel a: 2D line-of-sight column density map of CO_2 (in $10^{18} \text{ CO}_2/\text{m}^2$), Ganymede-leading side. Panel b: same as panel a but for the Ganymede-trailing side. Panel c: latitudinal variation of the longitudinal average column density for the Ganymede-leading side (for bins of 7.5° in latitude). Panel d: same as for panel c but for the Ganymede-trailing side and bins in latitude of 15° . Dark blue symbols: JWST observations. Light blue symbols: EGM simulation. Red symbols: JWST observations. Orange symbols: EGM simulation.

1166 L.4. Simulation of CO_2 sputtering on entire Ganymede's 1167 surface

1168 We also investigated CO_2 sputtering over the southern open-
1169 field-line region of the leading hemisphere and over the southern
1170 and northern open-field-line regions of the trailing hemisphere.
1171 This approach allowed us to illustrate how the sputtering ejection
1172 rate would need to be changed from a region to another to
1173 explain the JWST observations. The surface temperature of the
1174 trailing side was calculated using the same approach as for lead-
1175 ing side (see parameters of the thermal model in Appendix K).

Figure L.4 provides one example of results obtained by using 1176
the same q_{CO_2} and f_c values for the two hemispheres, the only 1177
difference being the location of the OCFBs. The distribution of 1178
sputtered CO_2 over the whole surface is described according to: 1179

- a region (1) of sputtering above a latitude of 50°N , with a 1180
flux of sputtered CO_2 molecules determined as described in 1181
section I, with $f_c = 640$ and $q_{\text{CO}_2} = 1\%$, 1182
- a region (2) in the northern hemisphere open field-lines re- 1183
gion with $f_c = 80$ and $q_{\text{CO}_2} = 1\%$ (e.g., describing regions 1184
between northern OCFB and $> 50^\circ\text{N}$ polar cap on the lead- 1185
ing hemisphere), 1186

- 1187 – a region (3) in the southern hemisphere open field-lines re- 1245
 1188 gion with $f_c = 60$ and $q_{\text{CO}_2} = 1\%$, 1246
 1189 – a region (4) in close field-lines region with $f_c = 0$. 1247

1190 Assuming the same $f_c = 640$ value for all regions, would be 1248
 1191 equivalent to adopting $q_{\text{CO}_2} = 1\%$, 0.13% , 0.09% , and 0% for 1249
 1192 regions (1), (2), (3), (4) respectively. With these assumptions, the 1250
 1193 shape of the latitudinal distribution observed on the leading side 1251
 1194 is reproduced but not that of the trailing side (Fig. L.4). Repro- 1252
 1195 ducing at least approximately Ganymede's CO₂ exosphere with 1253
 1196 the sputtering mechanism might be possible by adjusting f_c or 1254
 1197 q_{CO_2} parameters geographically over the surface. However, this 1255
 1198 model cannot explain the exospheric excess observed at equa- 1256
 1199 torial to mid latitudes in the southern regions of the trailing 1257
 1200 hemisphere (Fig. 1) taking into account that, at the time of the 1258
 1201 trailing-side observation, Ganymede was inside the plasma sheet 1259
 1202 of Jupiter's magnetosphere, so southern polar regions were not 1260
 1203 over-exposed to plasma bombardment with respect to northern 1261
 1204 regions (Appendix J). 1262

1205 Appendix M: PSF deconvolution of CO₂ gas map 1263

1206 In order to analyze the spatial distribution of the CO₂ ex- 1264
 1207 osphere on Ganymede's leading side in more detail, we 1265
 1208 applied a deconvolution procedure. The deconvolution pro- 1266
 1209 cess was done using the AIDA algorithm in classical mode 1267
 1210 (Hom et al. 2007) that requires science and PSF data files. 1268
 1211 Reported Full Width at Half Maximum (FWHM) measured 1269
 1212 at $4.25\ \mu\text{m}$ from JWST point-source observations range 1270
 1213 from 0.14 to $0.17''$ (Deugenio2023 and are expected to 1271
 1214 vary with the observational mode (e.g., number of dithers). 1272
 1215 Unfortunately, no reference star was observed during the 1273
 1216 observations of Ganymede, so we used the WebbPSF software 1274
 1217 ([https://www.stsci.edu/jwst/science-planning/](https://www.stsci.edu/jwst/science-planning/proposal-planning-toolbox/psf-simulation-tool)
 1218 [proposal-planning-toolbox/psf-simulation-tool](https://www.stsci.edu/jwst/science-planning/proposal-planning-toolbox/psf-simulation-tool)) 1275
 1219 which can calculate monochromatic PSFs for NIRSpec in spec- 1276
 1220 troscopic mode. PSFs were generated at various wavelengths to 1277
 1221 explore how deconvolved images vary with the PSF FWHM. 1278

1222 We show in Fig. M.1 the deconvolution of the CO₂ gas map 1279
 1223 above the leading hemisphere for PSFs with FWHMs of 0.165 , 1280
 1224 0.185 and $0.205''$ corresponding to WebbPSF outputs at 3.5 , 4.2 1281
 1225 and 5 microns, respectively. For this purpose, we used the CO₂ 1282
 1226 column density map derived for the full 37×43 spaxels IFU 1283
 1227 frame (i.e., including results outside Ganymede disk). The de- 1284
 1228 convolved maps were then reconvolved with the PSFs used for 1285
 1229 the deconvolution. Residuals with respect to the original data are 1286
 1230 shown in Fig. M.1 (bottom row) for the three assumed PSFs, and 1287
 1231 do not differ much. The deconvolved CO₂ gas distribution con- 1288
 1232 firms that the northern CO₂ excess is confined in longitude and 1289
 1233 latitude, and that the decrease of the column density above lati- 1290
 1234 tudes of 60°N is real. The deconvolved map also clearly shows 1291
 1235 the excess nearby the southern OCFB. 1292

1236 Appendix N: Spatial variations of surface CO₂ band 1293 1237 depth 1294

1238 The CO₂ absorption band around $4.26\ \mu\text{m}$ is widespread over 1295
 1239 the surface of Ganymede. Globally, the CO₂ band depth ap- 1296
 1240 pears anti-correlated with bond albedo and water ice absorp- 1297
 1241 tion band depths, with the maximum CO₂ band depth on the 1298
 1242 equatorial regions but much lower values on regions poleward 1299
 1243 of 30°N (Fig. N.1, Hibbitts et al. (2003), Paper I). The CO₂ 1300
 1244 band center (Fig. 4C) and shape show stronger relationship with

surface brightness for both hemispheres, redshifting and get- 1245
 ting narrower/asymmetric as we reach polar latitudes, respec- 1246
 tively. As discussed in Paper I these changes of band position 1247
 and shape may be due to contributions of CO₂ under varying 1248
 physical states/matrices depending on the latitude: adsorbed on 1249
 minerals or salts at the equatorial latitudes, and possibly mixed 1250
 in amorphous water ice at the poles (Fig. 4C). But why is the 1251
 CO₂ band depth weaker at the polar regions, where CO₂ gas 1252
 appears to be released from the surface? Actually, the poles of 1253
 Callisto also have weaker CO₂ band depths and finer-grained 1254
 water ice than the equatorial regions, just like Ganymede. From 1255
 Galileo/NIMS data, this was interpreted as fine-grained ice phys- 1256
 ically covering and spectrally masking the CO₂, although such 1257
 a masking effect was not demonstrated numerically or exper- 1258
 imentally (McCord et al. 1998; Hibbitts et al. 2000; Hibbitts 1259
 et al. 2003). JWST/NIRSpec data of Ganymede also show some 1260
 anti-correlation between the spatial distribution of the CO₂ band 1261
 depth and that of the H₂O $4.5\text{-}\mu\text{m}$ band depth (Fig. N.1). How- 1262
 ever, the lower CO₂ band depth at the polar regions may not be 1263
 (only) due to a putative spectral-masking effect, but to other fac- 1264
 tors. Maybe the surface areal abundance of CO₂ is lower within 1265
 the open-field-line areas because the irradiation releases it more 1266
 efficiently from its mineral association. As a result, CO₂ may 1267
 be less concentrated over non-ice mineral-rich terrains and only 1268
 present on bright ice-rich patches (the coldest surfaces), reduc- 1269
 ing its geographically averaged band depth and making its band 1270
 shape and position more compatible to CO₂ mixed in water ice. 1271
 Another explanation might also be that the absorption coeffi- 1272
 cient of CO₂ decreases at the poles because CO₂ is in a different 1273
 state/matrix and/or at a different temperatures than at equatorial 1274
 regions. 1275

1276 Despite the lack of correlation between the global distribu- 1277
 tion of CO₂ gas column density and solid CO₂ band depth, there 1278
 are some local areas where both are minimum (in the south polar 1279
 regions and in an area at about $260\text{-}300^\circ\text{W}$ and $30^\circ\text{S}\text{-}50^\circ\text{N}$, 1280
 Fig. N.1), and some spaxels at the extreme north of the leading 1281
 hemisphere show an enhanced CO₂ band depth (Fig. 4). 1282

1283 Appendix O: Additional figures 1284

1285

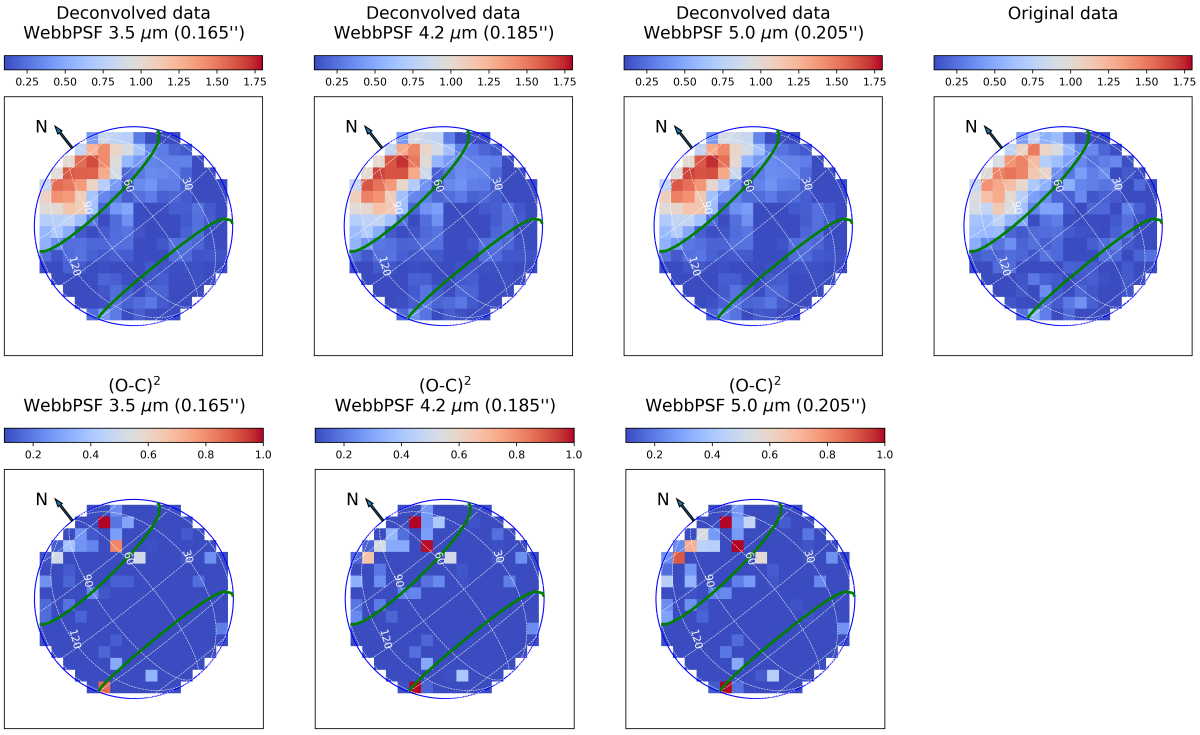


Fig. M.1. PSF deconvolution. Top: deconvolved CO_2 -gas maps (leading hemisphere) obtained with the AIDA algorithm using NIRSpec PSFs calculated with WebbPSF at $3.5 \mu\text{m}$ ($\text{FWHM} = 0.165''$), $4.2 \mu\text{m}$ ($\text{FWHM} = 0.185''$) and $5 \mu\text{m}$ ($\text{FWHM} = 0.205''$). Bottom: residuals of the deconvolution for each calculated PSF; plotted are $(O-C)^2$, where O is the original CO_2 column-density map (leading hemisphere, top-right plot), and C is the convolution of the deconvolved O map. Color bars are in unit of 10^{18}m^{-2} .

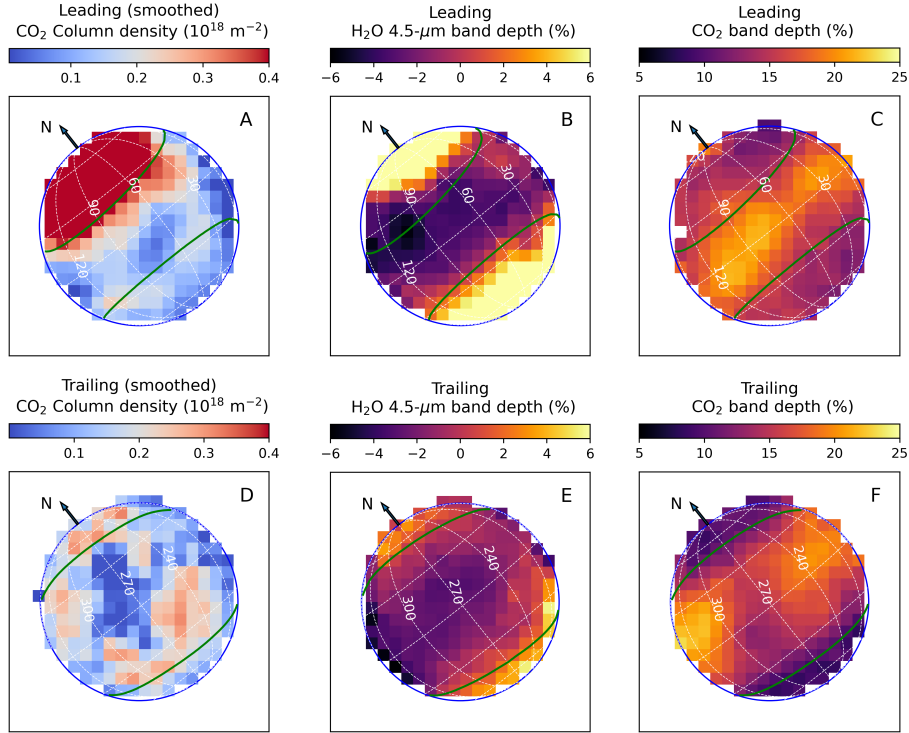


Fig. N.1. Comparing CO_2 exosphere to H_2O and CO_2 distribution on Ganymede's surface. Top and bottom rows are for the leading and trailing hemispheres, respectively. A, D: CO_2 gas column density maps at a 3×3 smoothed resolution (this work); B, E: H_2O band depth at $4.5 \mu\text{m}$ (Paper I); C, F: CO_2 -solid $4.3 \mu\text{m}$ band depth (Paper I). In these plots, unlike in Figs 1 and O.1, the same color scales and boxcar smoothing are used for leading and trailing.

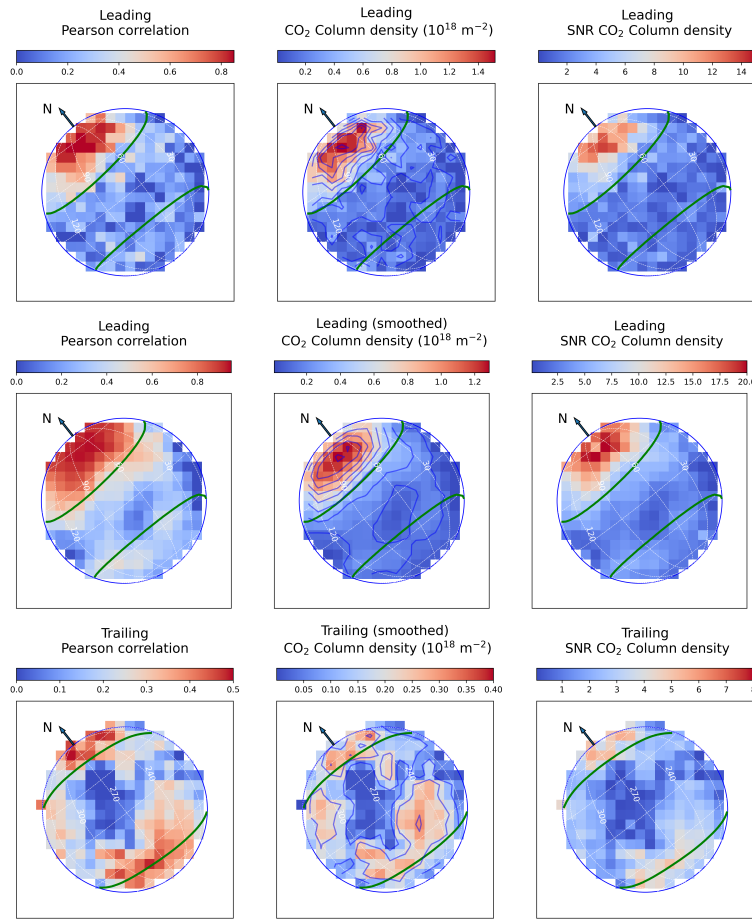


Fig. O.1. CO₂ gas distribution above Ganymede surface. First and second rows are for the leading side, at the original and 3×3 boxcar smoothed (for higher S/N) resolutions, respectively. Bottom row is for the trailing side at 3×3 smoothed resolution. Plots on the first column show the Pearson correlation coefficient between continuum-filtered residual CO₂ gas emission and a forward CO₂ fluorescence model at 105 K (Fig. H.1). Plots on the second and third column show the line-of-sight CO₂ column density and S/N inferred by fitting synthetic CO₂ fluorescence spectra (Appendix B). The color scales for the leading and trailing sides are different, and indicated above the plots. Pixel sizes are 0.1×0.1". The green lines show the open-closed field-line boundary Duling et al. (2022)

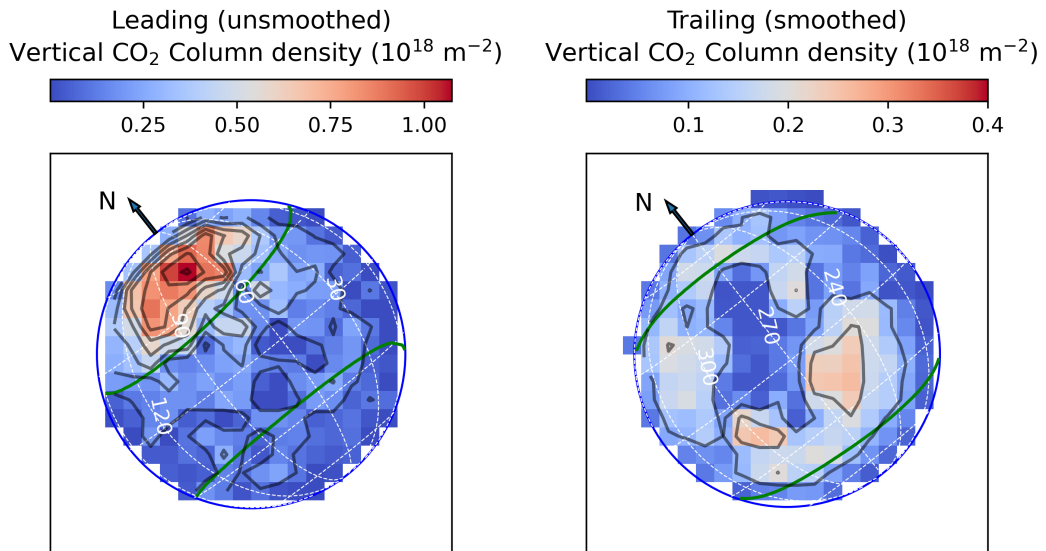


Fig. O.2. CO₂ vertical column density maps of the leading (left) and trailing (right) hemispheres. They were deduced from the line-of-sight column density maps, by multiplying them by the cosine of the angle between local zenith and line of sight directions. For the leading hemisphere, the central contour for the north excess is at about 72°W (12.6 h local time), 45°N. Trailing data were smoothed using a 3×3 boxcar filter.

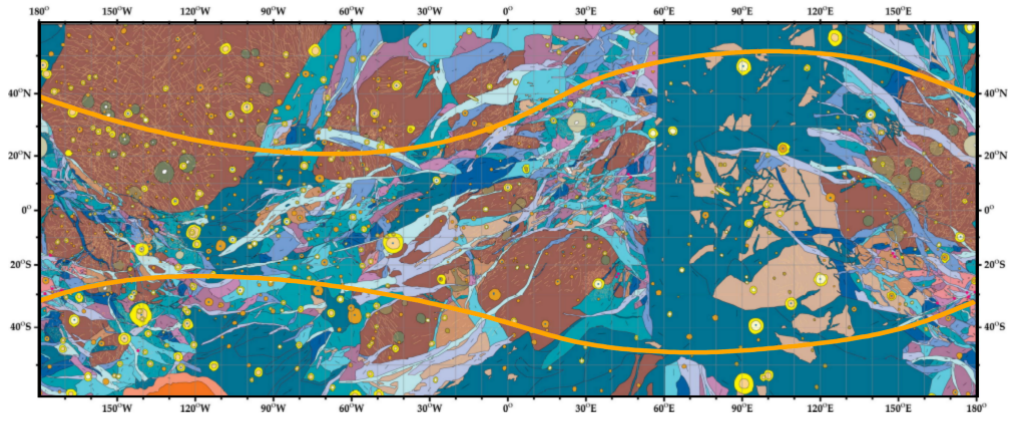


Fig. O.3. Geological map of Ganymede (Plate 2 of Patterson et al. (2010)). The green lines show the open-closed field-line boundary at the time of the JWST observations Duling et al. (2022).